

A jamming plane of sphere packings

Yuliang Jin^{1,2,3,*} and Hajime Yoshino^{3,4,†}

¹*CAS Key Laboratory of Theoretical Physics, Institute of Theoretical Physics,
Chinese Academy of Sciences, Beijing 100190, China*

²*School of Physical Sciences, University of Chinese Academy of Sciences, Beijing 100049, China*

³*Cybermedia Center, Osaka University, Toyonaka, Osaka 560-0043, Japan*

⁴*Graduate School of Science, Osaka University, Toyonaka, Osaka 560-0043, Japan*

The concept of jamming has attracted great research interest due to its broad relevance in soft-matter such as liquids, glasses, colloids, foams, and granular materials, and its deep connection to the sphere packing problem and optimization problems. Here we show that the domain of amorphous jammed states of frictionless spheres can be significantly extended, from the well-known jamming-point at a fixed density, to a jamming-plane that spans the density and shear strain axes. We explore the jamming-plane, via athermal and thermal simulations of compression and shear jamming, with a help of an efficient swap algorithm to prepare initial equilibrium configurations. The jamming-plane can be divided into reversible-jamming and irreversible-jamming regimes, based on the reversibility of the route from the initial configuration to jamming. Our results suggest that the irreversible-jamming behavior reflects an escape from the meta-stable glass basin to which the initial configuration belongs to, or the absence of such basins. All jammed states, either compression or shear jammed, are isostatic, and exhibit jamming criticality of the same universality class. However, the anisotropy of contact networks non-trivially depends on the jamming density and strain. Among all state points on the jamming-plane, the jamming-point is a unique one with the minimum jamming density and the maximum randomness. For lattice packings, the jamming-plane shrinks into a single shear jamming-line that is independent of initial configurations. Our study paves the way for solving the long-standing random close packing problem, and provides a more complete framework to understand jamming.

I. INTRODUCTION

In three dimensions, the densest packings of equal-sized spheres are the face-centered cubic (FCC) or the hexagonal close packing (HCP) lattices, whose densities (packing fractions) are $\varphi_{\text{FCC}} = \varphi_{\text{HCP}} \simeq 0.74$. This was conjectured initially by the celebrated scientist Kepler in the 17th-century, known as the Kepler conjecture, and was proved by mathematician Hales about 400 years later [1].

The “random version” of the sphere packing problem, however, remains unsolved. In the 1960th, based on the empirical observation that the packing fraction of ball bearings, when poured, shaken, or kneaded inside balloons, never exceeds a maximum value $\varphi_{\text{RCP}} \approx 0.64$, Bernal introduced the concept of *random close packing* (RCP) to characterize the optimal way to pack spheres randomly [2]. Although many experiments and simulations have reproduced random packings with a volume fraction around 0.64, an agreement on the exact value of φ_{RCP} has not been reached. Torquato et al. proposed that the idea of RCP should be replaced by a new notion called *maximally random jammed* (MRJ) state, where the randomness is measured by some order parameters which characterize the crystalline order [3]. O’Hern et al. designed a fast quench protocol which generates randomly jammed packings of monodisperse spheres at

$\varphi_{\text{J}} = 0.639 \pm 0.001$ in the thermodynamic limit [4], which is referred to as the jamming-point (J-point) [5]. Later, based on mean-field calculations, Zamponi and Parisi predicted that the jamming density of amorphous packings should span over a range on the jamming-line (J-line) [6], which has been supported in a number of numerical simulations [7–9].

Spheres can be constrained not only by compression but also by shear. In granular rheology, the volume (in isobaric processes) or the pressure (in isovolumetric processes) of an assembly of granular particles can increase under shear, known as Reynolds dilatancy [10, 11]. Indeed granular matter and suspensions can be jammed by shear [11–17]. However, previous studies found that, for frictionless spheres, shear jamming and isotropic jamming occur at the same density in the thermodynamic limit [18, 19]. In this paper, we show that this is not true in general. Based on extensive numerical simulations, we further show that the phase space of amorphous packings of frictionless spheres can be extended significantly from the J-point to a jamming-plane (J-plane). This objective is achieved by combining multiple jamming protocols (thermal/athermal, compression/shear), with the help of a swap algorithm [20] to generate initial equilibrium (liquid) configurations of hard spheres (HSs) thermalized at various densities φ_{eq} [9].

Since our approach extends the phase space of random packings to a non-conventional regime, the properties of the new states deserve to be analyzed in detail. Are shear jammed states reversible upon inverting the route to jamming [21]? Are shear jammed packings isostatic (i.e., the average contact number per particle is $z_{\text{J}} = 2d = 6$

* yuliangjin@mail.itp.ac.cn

† yoshino@cmc.osaka-u.ac.jp

in $d = 3$ dimensions) as in the isotropic jamming case [4, 22]? Do the isotropically jammed states obtained by compression and anisotropically jammed states created by shear exhibit critical properties of the same jamming universality class [23]? How do the anisotropy [12, 24] and the bond-orientational order [25] of the contact network change with the jamming strain? What is the difference on shear jamming between amorphous states and crystals? All these questions will be answered in this paper.

In experiments, colloidal suspensions and granular matter are two typically studied jamming systems. A colloidal suspension jams when the viscosity diverges [26, 27], while the jamming of granular matter occurs at the onset of rigidity [12, 28, 29]. The main difference between the two systems lies in the motion of particles. Granular particles are large enough such that their thermal motions can be neglected, which turns the system into athermal by nature. To numerically model suspensions of (hard) colloidal particles, we simulate thermal HSs following Newtonian molecular dynamics [3, 30]. To model granular materials, we simulate harmonic soft spheres (SSs) following overdamped quasistatic dynamics [4]. We neglect the effects of friction [12–14], adhesion [31], and hydrodynamic interactions [14], and use models with a large polydispersity to prevent crystallization [9, 20, 32]. Our numerical results are relevant to a number of simple but representative experimental jamming systems.

The paper is organized as follows. We first explain schematically the J-plane (Sec. II). Then we introduce the models (Sec. III) and the methods to prepare initial configurations (Sec. IV). We describe how to explore the J-plane using an athermal protocol in Sec. V, and a thermal protocol in Sec. VI. We next analyze the properties of packings on the J-plane, including the reversibility (Sec. VII), the isostaticity and the jamming universality (Sec. VIII), the anisotropy (Sec. IX), and the bond-orientational order (Sec. X). Finally we compare the J-plane of amorphous packings to its counterpart of crystals (Sec. XI), and conclude in Sec. XII.

II. SCHEMATIC JAMMING-PLANE

In this section, we briefly summarize the qualitative features of the J-plane (see Fig. 1). These features will be discussed in detail in the following sections.

- (i) **Jamming-plane.** Any amorphous packing of spheres, either compression jammed or shear jammed, can be described by a state point $\{\varphi_j, \gamma_j\}$ on the J-plane (Fig. 1), where φ_j is the jamming density and γ_j is the jamming strain. While Fig. 1 shows a schematic J-plane in the thermodynamic limit, quantitatively it may depend on model parameters such as the polydispersity. We do not consider partially ordered packings [3, 33] in the J-

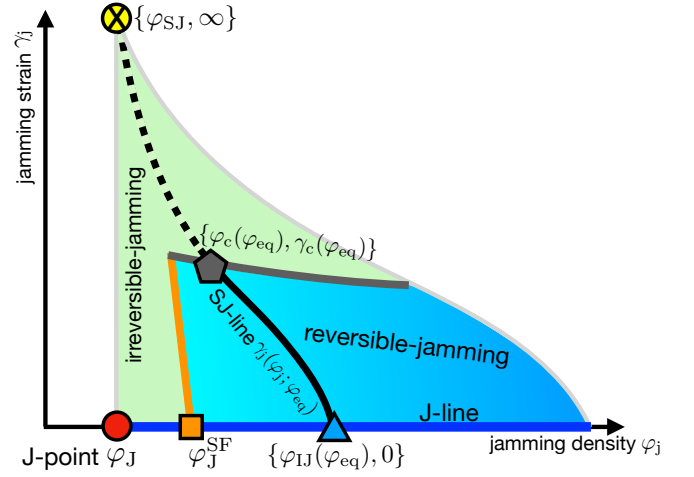


FIG. 1. Schematic J-plane. The J-plane (φ_j, γ_j) , which is extended from the J-point and the J-line, represents the region where the frictionless amorphous jammed configuration at density φ_j and strain γ_j exists. The J-plane is divided into reversible-jamming and irreversible-jamming regimes. Each state in the reversible-jamming regime can be related reversibly to the initially thermalized HS liquid state at $(\varphi_{eq}, 0)$. The lighter color in this region represents the smaller corresponding φ_{eq} . For each φ_{eq} , there is a SJ-line $\gamma_j(\varphi_j; \varphi_{eq})$ as indicated, whose end points are $\{\varphi_{IJ}(\varphi_{eq}), 0\}$ and $\{\varphi_{SJ} = \varphi_J, \infty\}$. The reversible-jamming regime is upper-bounded by the yielding-jamming separation line of thermal HSs $\{\varphi_c(\varphi_{eq}), \gamma_c(\varphi_{eq})\}$ (gray line), and left-bounded by the state-following line (orange line), whose end point is the state-following jamming point at $\{\varphi_J^{SF}, 0\}$. How the J-line and the J-plane are bounded from above is an open question.

plane, but in Sec. XI we discuss perfect FCC crystalline packings for a comparison.

- (ii) **Jamming-point.** The J-point [4] at $\{\varphi_J, 0\}$ can be identified as a special, unique point with the minimum density φ_J among all state points on the J-plane. The packings at the J-point can be generated by a fast compression from random initial configurations with $\varphi_{eq} = 0$ [4]. The vertical line $\{\varphi_j = \varphi_J, \gamma_j\}$ sets the leftmost boundary of the J-plane: no packing exists below the density φ_J .

- (iii) **Jamming-line.** The J-line $\{\varphi_{IJ}, 0\}$ with

$$\varphi_{IJ} = \varphi_{IJ}(\varphi_{eq}), \quad (1)$$

is formed by the state points of isotropic packings. In isotropic compression protocols, the jamming density φ_{IJ} depends on the density φ_{eq} of the initial configuration before compression, which is sampled from the equilibrium ensemble [7–9].

For clarity, let us note that there are other protocols to prepare initial configurations, equilibrated to certain extents, such as the cyclic compression [15] and the cyclic shear protocols [16]. For them, φ_{IJ} depends on parameters that are specific

to the protocols. In the cyclic compression protocol, $\varphi_{IJ}(\varphi^{\max})$ depends on the maximum over-compression density φ^{\max} [15]; in the cyclic shear protocol, $\varphi_{IJ}(\gamma^{\max})$ depends on the maximum shear strain γ^{\max} [16].

According to the mean-field theory [6], the J-line Eq. (1) is bounded from above by the *glass close packing* density, $\varphi_{GCP} = \varphi_{IJ}(\varphi_K)$, where φ_K is the Kauzmann point density. However, reaching this point is beyond the limit of any existing numerical protocols. In practice, the maximum jamming density φ_{IJ}^{\max} depends on the protocol efficiency. For example, athermal training protocols such as cyclic compression or cyclic shear typically give $\varphi_{IJ}^{\max} \approx \varphi_J + 0.02$ [15, 16]. In this study, we are able to reach much higher relative maximum jamming density $\varphi_{IJ}^{\max} \approx \varphi_J + 0.035$, thanks to the powerful swap algorithm for the preparation of the initial equilibrium configurations [9].

- (iv) **Shear jamming-lines (SJ-lines).** Each SJ-line

$$\gamma_j = \gamma_j(\varphi_j; \varphi_{eq}), \quad (2)$$

or equivalently,

$$\varphi_j = \varphi_j(\gamma_j; \varphi_{eq}), \quad (3)$$

represents the functional dependency between γ_j and φ_j for a given φ_{eq} . The states with a non-zero jamming strain γ_j are said to be *shear jammed*. The lower end point of the SJ-line at $\gamma_j = 0$ is nothing but an isotropic jamming point at $\{\varphi_{IJ}(\varphi_{eq}), 0\}$ on the J-line Eq. (1),

$$\varphi_{IJ}(\varphi_{eq}) = \varphi_j(0; \varphi_{eq}), \quad (4)$$

and the upper end point is at $\{\varphi_{SJ} = \varphi_J, \gamma_j = \infty\}$ where all SJ-lines meet. The J-plane contains infinite number of SJ-lines, but in simulations we will use a few typical SJ-lines to represent the J-plane.

- (v) The J-plane is divided into two regions.

- **Reversible-jamming regime** : This regime contains jammed states that can be generated by reversible routes, in the sense that the initial unjammed state at $(\varphi_{eq}, 0)$ and the final jammed state at (φ_j, γ_j) are in the same meta-stable glass basin (or meta-basin) and therefore the initial memory is kept. The approach to jamming in this regime corresponds to the so-called *state-following* dynamics in structural [34, 35] and spin [36–40] glasses.
- **Irreversible-jamming regime** : In this regime the routes to jamming are irreversible, in the sense that the initial unjammed state and the final shear jammed state are in different meta-stable glass basins. The memory of the initial condition is partially or completely lost. Very importantly, the J-point belongs to this regime.

The two regimes are separated by two lines: the **yielding-jamming separation line** formed by state points $\{\varphi_c(\varphi_{eq}), \gamma_c(\varphi_{eq})\}$, which separates shear yielding and shear jamming in thermal HSs, and the **state-following line** that separates state-following and non-state-following dynamical regimes. The end point of the state-following line is the state-following jamming point at $\{\varphi_J^{SF}, 0\}$, which is compression quenched from the state-following density φ_{SF} , i.e., $\varphi_J^{SF} = \varphi_{IJ}(\varphi_{eq} = \varphi_{SF})$.

- (vi) Properties of states on the jamming-plane : **isostaticity, jamming universality, anisotropy, and bond-orientational order.** Any state point $\{\varphi_j, \gamma_j\}$ on the J-plane corresponds to an isostatic jamming-unjamming transition [4]. Keeping the strain γ_j unchanged, the packing becomes over-jammed under a compression from φ_j to $\varphi = \varphi_j + \delta\varphi$, where $\delta\varphi > 0$, and unjammed under a decompression from φ_j to $\varphi = \varphi_j - \delta\varphi$. Quite remarkably, the isotropically jammed and shear jammed states belong to the same universality class: the jamming critical exponents near φ_j , from both below and above jamming, are independent of γ_j (including the case $\gamma_j = 0$). However, shear jammed states are anisotropic. For large φ_{eq} , the anisotropic parameter changes non-monotonically with γ_j along the SJ-line, associated with a non-trivial change of the contact angle distribution. Among all state points on the J-plane, the J-point is also special in the sense that it has the minimum bond-orientational order.

III. MODELS

The systems consist of N spherical particles in a simulation box of volume V , for a continuous diameter distribution $P(D) \sim D^{-3}$, where $D_{\min} \leq D \leq D_{\min}/0.45$ [20]. The number density is $\rho = N/V$ and the volume fraction is $\varphi = \rho(4/3)\pi\bar{D}^3$. The mean diameter \bar{D} is set as the unity of length, and all particles have the same unit mass $m = 1$. For the same $P(D)$, two models are studied.

- (i) **Thermal hard sphere (HS) model.** The model represents a suspension of hard colloidal particles with negligible friction. The simulation is performed under constant unit temperature $T = 1$. Because the potential energy is always zero and only inter-particle collisions contribute, both pressure P_{entro} and stress Σ_{entro} are purely *entropic*. We define the reduced entropic pressure as $p_{\text{entro}} = P_{\text{entro}}V/Nk_B T$ and the reduced entropic stress as $\sigma_{\text{entro}} = \Sigma_{\text{entro}}V/Nk_B T$, and set the Boltzmann constant $k_B = 1$. The method to compute p_{entro} and σ_{entro} is explained in detail in Ref. [41]. Jamming occurs when the entropic pressure and stress diverge.

- (ii) **Athermal soft sphere (SS) model.** The model represents a frictionless granular system. The SS potential has a harmonic form $U(r_{ij}) = \frac{1}{2}(1 - r_{ij}/D_{ij})^2$ (zero if $r_{ij} > D_{ij}$), where r_{ij} is the inter-particle distance between particles i and j , and $D_{ij} = (D_i + D_j)/2$ is the mean diameter. The simulation is performed at zero temperature. Both pressure P_{mech} and stress Σ_{mech} are contributed by the mechanical contacts between particles, and therefore are purely *mechanical*. The SSs are jammed if $P_{\text{mech}} > 0$, and the unjamming transition occurs as $P_{\text{mech}} \rightarrow 0$.

IV. METHOD TO PREPARE INITIAL CONFIGURATIONS

To be used as the initial states, we generate equilibrium liquid configurations of the thermal HS model at $\varphi_{\text{eq}} > 0$, as well as purely random (ideal gas) configurations at $\varphi_{\text{eq}} = 0$. Note that, the HS liquid configuration at the low-density limit is identical to the ideal gas configuration, because the excluded volume effect is negligible. To use these initial configurations in the athermal protocol (sec. V), we simply need to replace the thermalized HSs by SSs at the same positions, and switch off the temperature.

The initial configurations with $\varphi_{\text{eq}} > 0$ are prepared using a swap algorithm [20]. At each swap Monte Carlo step, two randomly chosen particles are swapped if they do not overlap with other particles at the new positions. The swap moves are integrated with event-driven molecular dynamics [21, 41], which significantly facilitates the equilibration procedure. The diameter distribution $P(D)$ (see Sec. III) was designed to optimize the efficiency of the swap algorithm [42]. This algorithm allows us to equilibrate HS systems over a wide range of volume densities, $\varphi_{\text{eq}} \in [0, 0.655]$. For several chosen φ_{eq} in this range, we prepare equilibrium configurations for a few different system sizes $N = 250, 500, 1000, 2000, 4000, 8000$. For each N , 500-2000 independent samples are generated, in order to obtain sufficient statistics. The continuous polydispersity highly suppresses crystallization [32, 43]. The crystalline order is absent in all equilibrium configurations considered in this study. However, in Sec. XI we study perfect FCC packings for a comparison.

The equilibrium liquid equation of state (EOS) $p_{\text{entro}}^L(\varphi_{\text{eq}})$ can be well described by the empirical Carnahan-Stirling form [44] (see Fig. 2). The non-equilibrium glass EOS $p_{\text{entro}}^G(\varphi; \varphi_{\text{eq}})$ depends on the glass transition density $\varphi_g = \varphi_{\text{eq}}$, where the system falls out of equilibrium [44]. In practice this is obtained by the thermal compression (TC) protocol explained in sec. VI: the standard event-driven molecular dynamics without swap are used to simulate the compression process. The dynamical glass transition crossover density (or the mode-coupling theory MCT crossover density) is $\varphi_d = 0.594(1)$ [44]. The onset density of the glassy dy-

TABLE I. Summary of relevant densities for the model, including the dynamical glass transition crossover density φ_d , the onset density φ_{onset} of glassy dynamics, the J-point density φ_J , the minimum isotropic jamming density $\varphi_{\text{IJ}}^{\text{min,th}}$ obtained by the thermal protocol, the state-following density φ^{SF} , and the state-following jamming density φ_J^{SF} .

φ_d [44]	φ_{onset} [32]	φ_J	$\varphi_{\text{IJ}}^{\text{min,th}}$	φ^{SF}	φ_J^{SF}
0.594(1)	0.56	0.655(1)	0.665	0.60	0.67

namics is $\varphi_{\text{onset}} \approx 0.56$, above which the time decay of correlation functions is non-exponential [32]. See Table I for a summary of relevant densities for the model.

V. EXPLORING THE JAMMING-PLANE USING AN ATHERMAL PROTOCOL

A. Athermal protocol

In this section, we explain how we explore the J-plane numerically using an athermal protocol, which combines (i) athermal rapid compression (ARC) [4], which is equivalent to rapid quench, and (ii) athermal quasistatic shear (AQS) [19] (see Fig. 2).

- (i) **Athermal rapid compression.** First, we instantaneously switch off the temperature of a HS equilibrium configuration at φ_{eq} . We then work at zero temperature using the SS inter-particle potential. The particle sizes are inflated or deflated proportionally and instantaneously to match a target density φ_j . Overlaps between particles are removed by minimizing the total potential energy using the FIRE algorithm [45]. The $\varphi_{\text{eq}} = 0$ limit of this procedure is exactly the well-known jamming algorithm introduced by O'Hern et al. [4] to study the J-point.
- (ii) **Athermal quasistatic shear.** If the configuration is not jammed after the previous step, we further apply AQS to the unjammed configuration. A simple shear deformation in the x - z direction is applied under Lees-Edwards boundary conditions [46]. At each step, all particles are shifted instantaneously by $x_i \rightarrow x_i + \delta\gamma z_i$, where x_i and z_i are the x - and z -coordinates of particle i , and $\delta\gamma$ is the strain step size, followed by the FIRE algorithm to remove the overlaps. The AQS is stopped either when the system is jammed at a certain jamming strain γ_j , or the strain γ exceeds a maximum value γ_{max} . The parameter values, $\delta\gamma = 0.02$ and $\gamma_{\text{max}} = 0.4$ (unless otherwise specified), are the same as in Ref. [19]. The $\varphi_{\text{eq}} = 0$ limit of this procedure is equivalent to the one employed in [19].

Criterion of athermal jamming. We use the same jamming criterion as in Ref. [4]. A system is unjammed if

the potential energy per particle $e_{\text{mech}} = E_{\text{mech}}/N$ decays below 10^{-16} after the energy minimization; it is jammed if $e_{\text{mech}} > 10^{-16}$ and the difference δe_{mech} between successive steps is less than 10^{-15} . The same criterion is applied to both isotropic and shear jamming that we discuss below.

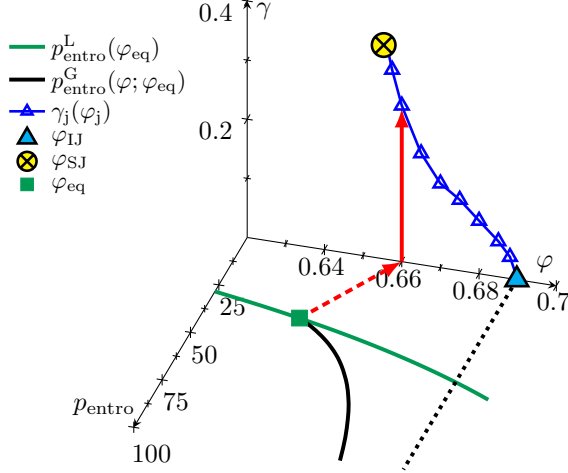


FIG. 2. Illustration of the athermal protocol. The example shows how a shear jammed packing of $N = 8000$ SSs is obtained, starting from a thermalized initial state at density $\varphi = \varphi_{\text{eq}}$ and zero strain. The entropic pressure and density of the initial state are related by the liquid EOS $p_{\text{entro}}^L(\varphi_{\text{eq}})$. After switching off the temperature, the system is athermally compressed from $\varphi_{\text{eq}} = 0.643$ to the target density $\varphi = 0.660$ (red dotted arrow line), and then is shear jammed at $\gamma = 0.259$ by using AQS (red solid arrow line). This jammed state is described by a state point $\{\varphi_J = 0.660, \gamma_J = 0.259\}$ on the J-plane.

Now we are ready to explore the J-plane by the athermal protocol. We generate a large number of isotropically jammed (ARC) or shear jammed (ARC + AQS) packings, starting from independent samples of initial configurations at $\{\varphi_{\text{eq}}, 0\}$. For each of them, we precisely locate the state point $\{\varphi_J, \gamma_J\}$ at which the system becomes jammed based on the criterion described above. For a given $\{\varphi_{\text{eq}}, 0\}$, we will find fluctuations of $\{\varphi_J, \gamma_J\}$ among samples, which strongly depends on the system size N . We will analyze carefully finite size effects to extract typical behaviors in the thermodynamic limit $N \rightarrow \infty$.

B. Jamming-point

To determine the J-point (see Fig. 1) of our model, we follow the standard procedure as in [4, 19], by applying ARC (rapid quench) to random initial configurations ($\varphi_{\text{eq}} = 0$), and extrapolating the jamming density in the thermodynamical limit $N \rightarrow \infty$ from a finite-size scaling analysis. We used 2000 samples of initial configurations at $\varphi_{\text{eq}} = 0$ in the following analysis.

We denote by $f_{\text{IJ}}(\varphi_J, N, \varphi_{\text{eq}})$ the fraction of isotropically jammed realizations at density φ_J , for given N and φ_{eq} (for the sake of generality, φ_{eq} is expressed as a parameter). As shown in Fig. 3(a) (for the case of $\varphi_{\text{eq}} = 0$), the fraction shows a finite size effect. We fit $f_{\text{IJ}}(\varphi_J, N, \varphi_{\text{eq}})$ to the form,

$$f_{\text{IJ}}(\varphi_J, N, \varphi_{\text{eq}}) = \frac{1}{2} + \frac{1}{2} \text{erf} \left\{ [\varphi_J - \varphi_{\text{IJ}}(N, \varphi_{\text{eq}})] / w_{\text{IJ}}(N, \varphi_{\text{eq}}) \right\}, \quad (5)$$

where $\text{erf}(x)$ is the error function, and $\varphi_{\text{IJ}}(N, \varphi_{\text{eq}})$ and $w_{\text{IJ}}(N, \varphi_{\text{eq}})$ are fitting parameters. The fitting is shown in Fig. 3(a) by solid lines.

The jamming density $\varphi_{\text{IJ}}(N, \varphi_{\text{eq}})$ (see Fig. 3(c) and Fig. 4(a)), and the width $w_{\text{IJ}}(N, \varphi_{\text{eq}})$ (see Fig. 4(d)) show finite size effects. We then fit $\varphi_{\text{IJ}}(N, \varphi_{\text{eq}})$ and $w_{\text{IJ}}(N, \varphi_{\text{eq}})$ to the finite-size scaling forms

$$\varphi_{\text{IJ}}(N, \varphi_{\text{eq}}) = \varphi_{\text{IJ}}^\infty(\varphi_{\text{eq}}) - aN^{-\mu_{\text{IJ}}}, \quad (6)$$

and

$$w_{\text{IJ}}(N, \varphi_{\text{eq}}) = bN^{-\omega_{\text{IJ}}} \quad (7)$$

where $\varphi_{\text{IJ}}^\infty(\varphi_{\text{eq}})$, a (which depends on φ_{eq}), μ_{IJ} , b (which depends on φ_{eq}) and w_{IJ} are fitting parameters. The fittings are shown by solid lines in Fig. 3(c), Fig. 4(a) and (d), and the values of $\varphi_{\text{IJ}}^\infty(\varphi_{\text{eq}})$, μ_{IJ} and ω_{IJ} are listed in Table II.

The J-point density for our model is $\varphi_J \equiv \varphi_{\text{IJ}}^\infty(\varphi_{\text{eq}} = 0) = 0.655(1)$, which is consistent with the value reported in Ref. [9]. In the thermodynamic limit, because $\omega_{\text{IJ}} > 0$, $f_{\text{IJ}}(\varphi_J, N, \varphi_{\text{eq}})$ becomes a step function of φ_J which jumps at $\varphi_J = \varphi_{\text{IJ}}^\infty(\varphi_{\text{eq}})$. Our results $\mu_{\text{IJ}} = 0.49(1)$ and $\omega_{\text{IJ}} = 0.45(1)$ are compatible with the values $\mu_{\text{IJ}} = 0.47(5)$ and $\omega_{\text{IJ}} = 0.55(3)$ reported in [4] for monodisperse spheres. Note that the exponent μ_{IJ} is related to the correlation length exponent ν in [4] by $\mu_{\text{IJ}} = d\nu$, where $d = 3$ is the dimension.

C. Jamming-line

As demonstrated in Refs. [8, 9], the J-point at φ_J can be extended into a J-line Eq. (1) by replacing the initial random configurations ($\varphi_{\text{eq}} = 0$) with dense equilibrium configurations ($\varphi_{\text{eq}} > 0$), before applying ARC. Figure 5 shows the dependence of $\varphi_{\text{IJ}}(N, \varphi_{\text{eq}})$ on φ_{eq} , for two different N . Below the onset density $\varphi_{\text{onset}} \approx 0.56$, the isotropic jamming density φ_{IJ} is nearly a constant; above φ_{onset} , it increases monotonically with φ_{eq} [8, 9]. For $\varphi_{\text{eq}} \in [0, \varphi_{\text{eq}}^{\text{max}}]$, we generate jammed packings on a J-line covering a range of densities, $\varphi_{\text{IJ}} \in [\varphi_{\text{IJ}}^{\text{min,ath}}, \varphi_{\text{IJ}}^{\text{max,ath}}]$. In the thermodynamical limit, the lower bound is set by the J-point density, $\varphi_{\text{IJ}}^{\text{min,ath}} = \varphi_J$, as discussed in Sec. VB. The maximum jamming density $\varphi_{\text{IJ}}^{\text{max,ath}} = \varphi_{\text{IJ}}(\varphi_{\text{eq}}^{\text{max}})$ depends on the maximum equilibrium density that we are able to reach in the protocol of preparing initial configurations. In this study, we obtain $\varphi_{\text{eq}}^{\text{max}} = 0.655$

TABLE II. Numerical values of densities φ_{IJ}^∞ , φ_{SJ}^∞ , φ_c^∞ , and of exponents μ_{IJ} , μ_{SJ} , μ_c , ω_{IJ} , ω_{SJ} , ω_c for two different φ_{eq} .

φ_{eq}	φ_{IJ}^∞	φ_{SJ}^∞	φ_c^∞	μ_{IJ}	μ_{SJ}	μ_c	ω_{IJ}	ω_{SJ}	ω_c
0	0.655(1)	0.657(1)	-	0.49(1)	0.46(1)	-	0.45(1)	0.48(1)	-
0.643	0.690(1)	0.657(1)	0.674(1)	0.6(1)	0.46(3)	0.48(5)	0.51(2)	0.35(1)	0.22(2)

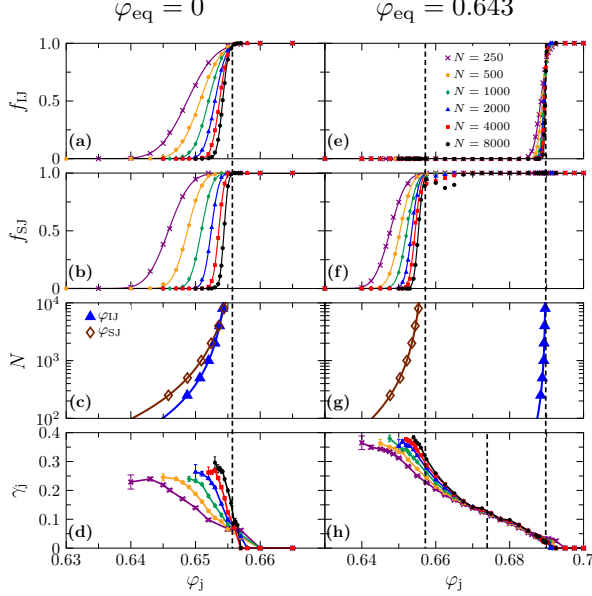


FIG. 3. System-size dependence of isotropic/shear jamming in the athermal protocol. (a-d) Data for which the initial states are random configurations, $\varphi_{eq} = 0$. (a) The fraction of isotropic jamming $f_{IJ}(\varphi_j, N, \varphi_{eq} = 0)$ and (b) the fraction of shear jamming $f_{SJ}(\varphi_j, N, \varphi_{eq} = 0)$ are plotted as functions of φ_j , for a few different N (points). The data points are fitted to Eqs. (5) and (8) (lines). (c) Fitting $\varphi_{IJ}(N, \varphi_{eq} = 0)$ and $\varphi_{SJ}(N, \varphi_{eq} = 0)$ to the scaling forms Eq. (6) and (9) (see Table II for the fitting parameters) shows that $\varphi_{IJ}^\infty(\varphi_{eq} = 0) \simeq \varphi_{SJ}^\infty(\varphi_{eq} = 0)$ within the numerical accuracy (see Fig. 4 for the log-log plots). The vertical dashed line represents $\varphi_J = 0.655(1)$. (d) The shear jamming strain γ_j is plotted as a function of φ_j for a few different N . (e-h) Same as (a-d) but for $\varphi_{eq} = 0.643$. The vertical dashed lines represent $\varphi_J = 0.655(1)$, $\varphi_c^\infty(\varphi_{eq} = 0.643) = 0.674(1)$, and $\varphi_{IJ}^\infty(\varphi_{eq} = 0.643) = 0.690(1)$ (see Table II). The data for the same N are represented by the same color in (a-b, d-f, h). The error bars represent standard errors in this paper.

for $N = 1000$, and $\varphi_{eq}^{\max} = 0.643$ for $N = 8000$, corresponding to $\varphi_{IJ}^{\max, \text{ath}} = 0.695$ and $\varphi_{IJ}^{\max, \text{ath}} = 0.690$ respectively [44].

Not only the J-point ($\varphi_{eq} < \varphi_{onset}$), but also any other point ($\varphi_{eq} > \varphi_{onset}$) on the J-line satisfies the finite-size formulas Eqs. (5), (6) and (7). In Fig. 3(e) and Fig. 4(b) and (e), we show an example with $\varphi_{eq} = 0.643$. Our results are compatible with $\mu_{IJ} \approx \mu_{SJ} \approx \omega_{IJ} \approx \omega_{SJ} \approx 0.5$ [19], which is independent of φ_{eq} (see Table II). We used 500 samples of initial configurations at $\varphi_{eq} = 0.643$ in the analysis.

D. Jamming-plane: the collection of shear-jamming lines

The J-plane is extended from the J-line by including shear jammed states. Starting from the remaining $1 - f_{IJ}(\varphi_j, N, \varphi_{eq})$ fraction of unjammed configurations after the ARC procedure, we apply AQS that stops either when the system jams or the strain exceeds γ_{\max} . We denote by $f_{SJ}(\varphi_j, N, \varphi_{eq})$ the fraction of configurations that jam under shear, and by $\gamma_j(\varphi_j, N, \varphi_{eq})$ the average jamming strain. In total, there are a fraction of $(1 - f_{IJ})(1 - f_{SJ})$ samples do not jam even at $\gamma = \gamma_{\max}$. Similarly to the isotropic jamming case Eq. (5), we fit the fraction of shear jamming $f_{SJ}(\varphi_j, N, \varphi_{eq})$ to the form

$$f_{SJ}(\varphi_j, N, \varphi_{eq}) = \frac{1}{2} + \frac{1}{2} \text{erf} \left\{ [\varphi_j - \varphi_{SJ}(N, \varphi_{eq})] / w_{SJ}(N, \varphi_{eq}) \right\}, \quad (8)$$

and use the finite-size scalings

$$\varphi_{SJ}(N, \varphi_{eq}) = \varphi_{SJ}^\infty(\varphi_{eq}) - aN^{-\mu_{SJ}} \quad (9)$$

and

$$w_{SJ}(N, \varphi_{eq}) = bN^{-\omega_{SJ}} \quad (10)$$

to estimate $\varphi_{SJ}^\infty(\varphi_{eq})$, μ_{SJ} and ω_{SJ} (see Table II for the values).

1. Shear jamming for $\varphi_{eq} = 0$

Let us first discuss the case of $\varphi_{eq} = 0$ for shear jamming. Note that as long as $\varphi_{eq} < \varphi_{onset}$, the behavior of isotropic jamming (Fig. 5), as well as shear jamming, is independent of φ_{eq} . The fittings of Eqs. (8), (9) and (10) are included in Fig. 3(b), Fig. 4(a) and (d). According to the values listed in Table II, we find that $\varphi_{IJ}^\infty(\varphi_{eq} = 0) \simeq \varphi_{SJ}^\infty(\varphi_{eq} = 0) \simeq \varphi_J$ within the numerical error. Therefore, isotropic jamming and shear jamming occur at the same density in the thermodynamical limit, which is consistent with Ref. [19]. However, we do not exclude the possibility that there is a small difference, which is in the order of 0.001, between the isotropic jamming density $\varphi_{IJ}^\infty(\varphi_{eq} = 0)$ and the shear jamming density $\varphi_{SJ}^\infty(\varphi_{eq} = 0)$, in the thermodynamical limit. The scaling exponents used in the finite-size scaling Eqs. (6), (7), (9) and (10) are also approximately identical, $\mu_{IJ} \approx \mu_{SJ} \approx \omega_{IJ} \approx \omega_{SJ} \approx 0.5$ [19].

Since $\varphi_{IJ}^\infty(\varphi_{eq} = 0) = \varphi_{SJ}^\infty(\varphi_{eq} = 0)$, the SJ-line Eq. (2) should be vertical in the thermodynamical limit [18, 19], which is consistent with the trend seen in Fig. 3(d). In

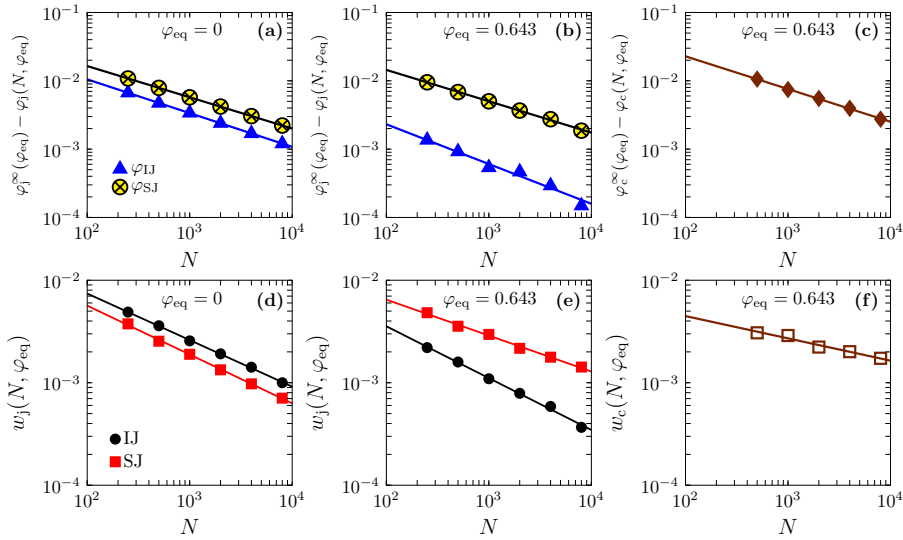


FIG. 4. Finite-size scaling. The isotropic and shear jamming densities obtained by the athermal protocol are fitted according to the scaling forms Eqs. (6) and (9) for (a) $\varphi_{\text{eq}} = 0$, (b) $\varphi_{\text{eq}} = 0.643$; their fluctuations are fitted according to Eqs. (7) and (10) for (d) $\varphi_{\text{eq}} = 0$, (e) $\varphi_{\text{eq}} = 0.643$. (c) The yielding-jamming separation density φ_c in thermal HSs and (f) its fluctuation are fitted according to Eqs. (13) and (14) for $\varphi_{\text{eq}} = 0.643$.

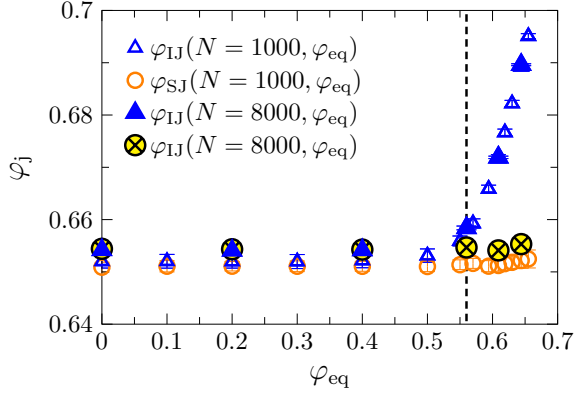


FIG. 5. Isotropic jamming density φ_{IJ} and shear jamming density φ_{SJ} as functions of φ_{eq} , for $N = 1000$ and 8000 , obtained by the athermal protocol. The onset density $\varphi_{\text{onset}} \approx 0.56$ is marked by the vertical dashed line. We used 200 – 2000 independent samples for each φ_{eq} here.

fact, we can show that the SJ-lines $\gamma_j(\varphi_j, N, \varphi_{\text{eq}} = 0)$ collapse onto a master curve $\gamma_j[(\varphi_j - \varphi_{\text{SJ}}^\infty)N^\mu, \varphi_{\text{eq}} = 0]$, with $\mu = 1/2$ (see Fig. 6), as suggested in Ref. [19]. The dependence of the SJ-line on the protocol parameter γ_{max} further indicates that the SJ-line extends to infinite strain $\gamma_j \rightarrow \infty$ in the limit $\gamma_{\text{max}} \rightarrow \infty$ (Fig. 6 inset).

2. Shear jamming for $\varphi_{\text{eq}} > \varphi_{\text{onset}}$

We next discuss the case of $\varphi_{\text{eq}} = 0.643$ (Fig. 3e-h), as an example for $\varphi_{\text{eq}} > \varphi_{\text{onset}}$. In contrast to the previous case ($\varphi_{\text{eq}} = 0$), the shear jamming density is

unambiguously lower than the isotropic jamming density in the thermodynamic limit, $\varphi_{\text{SJ}}^\infty(\varphi_{\text{eq}} = 0.643) < \varphi_{\text{IJ}}^\infty(\varphi_{\text{eq}} = 0.643)$ (see Table II for the values), and the SJ-line $\gamma_j(\varphi_j, N \rightarrow \infty, \varphi_{\text{eq}} = 0.643)$ does not tend to be vertical (Fig. 3h). The exponents $\mu_{\text{IJ}} \approx \mu_{\text{SJ}} \approx 0.5$ are independent of φ_{eq} within the numerical accuracy, while ω_{SJ} is slightly smaller than $\omega_{\text{IJ}} \approx 0.5$ (see Fig. 3(f), Fig. 4(b, e) and Table II).

We then extend our analysis more systematically to general values of φ_{eq} . As shown in Fig. 5, $\varphi_{\text{SJ}}(N, \varphi_{\text{eq}})$ is nearly a constant as a function of φ_{eq} . Figure 5 also shows that $\varphi_{\text{IJ}} \simeq \varphi_{\text{SJ}}$ when φ_{eq} is below $\varphi_{\text{onset}} \approx 0.56$, and $\varphi_{\text{IJ}} > \varphi_{\text{SJ}}$ above. These results indicate that, for $\varphi_{\text{eq}} > \varphi_{\text{onset}}$, shear jamming could occur over a range of densities $\varphi_j \in [\varphi_{\text{SJ}}, \varphi_{\text{IJ}}]$. This newly discovered region extends the phase space of jamming to a J-plane. In Fig. 7, we plot the SJ-lines Eq. (2), for a few different φ_{eq} to represent the J-plane.

VI. EXPLORING THE JAMMING-PLANE USING A THERMAL PROTOCOL

A. Thermal protocol

Jammed configurations can be obtained alternatively by applying (i) thermal compression (TC) and (ii) thermal quasi-static shear (TQS) to HSs [3, 22] (see Fig. 8).

- (i) **Thermal compression.** To simulate the TC procedure, we use the Lubachevsky-Stillinger algorithm [47], which is based on event-driven molecular dynamics. Starting from an equilibrium configuration at φ_{eq} , the algorithm compresses HSs by in-

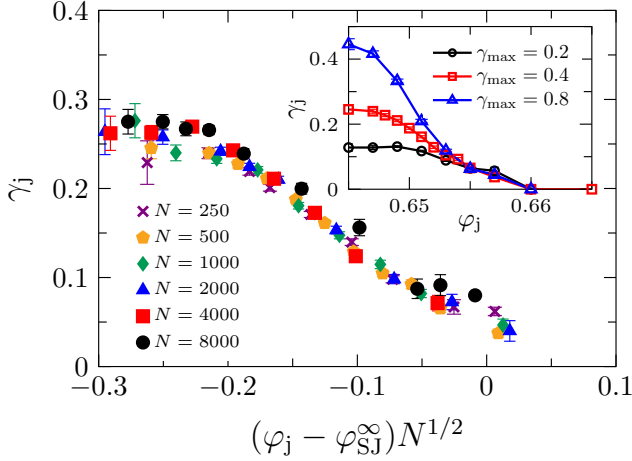


FIG. 6. Collapse of SJ-lines obtained by the athermal protocol, for $\varphi_{eq} = 0$ and a few different N , where $\varphi_{SJ}^\infty = 0.657$ is used (see Table II). (inset) The SJ-line, for $\varphi_{eq} = 0$ and $N = 500$, becomes steeper with increasing γ_{max} .

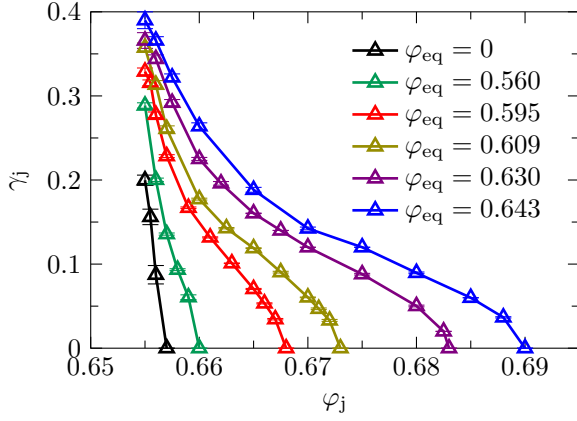


FIG. 7. J-plane obtained by the athermal protocol ($N = 8000$), represented by typical SJ-lines $\gamma_j(\varphi_j; \varphi_{eq})$ for a few different φ_{eq} (we only show the part for $\varphi_j > \varphi_{SJ}$ which means that $f_{SJ} > 0.5$).

flating their sizes with a fixed rate $\Gamma = \frac{1}{2D} \frac{dD}{dt}$. The simulation time is expressed in unit of $\sqrt{1/k_B m \bar{D}^2}$.

Although here Γ and φ_{eq} are treated as independent control parameters, in principle they play equivalent roles. Both of them control the glass transition density φ_g , which eventually determines the jamming density φ_{IJ} [44]. If $\varphi_{eq} = 0$ and swaps are switched off (as in the conventional Lubachevsky-Stillinger algorithm), then φ_g only depends on the compression rate Γ . In this case, the maximum φ_g is around the dynamical glass transition crossover density $\varphi_d = 0.594$, obtained by the slowest compression ($\Gamma \sim 10^{-6}$) that can be achieved in our simulations. If the swaps are switched on, then the maximum φ_g depends on the maximum equilibrium

density $\varphi_{eq}^{max} \approx 0.655$ that can be achieved by the swap algorithm, which is significantly higher than φ_d . For $\varphi_{eq} > \varphi_d$, the glass transition density φ_g , as well as the jamming density φ_{IJ} , mainly depends on φ_{eq} rather than on Γ (see below for a detailed analysis).

- (ii) **Thermal quasi-static shear.** To simulate shear, we apply constant volume simple shear in the x - z direction with a fixed rate $\dot{\gamma} = 10^{-4}$. For $\varphi_{eq} > \varphi_d$, the stress-strain curves are insensitive to the variation of $\dot{\gamma}$ for a few orders of magnitude [41]. At each step, we perform 1000 collisions per particle, and then instantaneously increase the shear strain by $\delta\gamma = \dot{\gamma}\delta t$, where δt is the time elapsed during the collisions. All particles are shifted by $x_i \rightarrow x_i + \delta\gamma z_i$. To remove the possible overlaps introduced during this shift, we switch to the SS potential and use the FIRE algorithm to minimize the energy. The SS potential is switched off after. As in the thermal protocol, Lees-Edwards boundary conditions are used.

Criterion of thermal jamming. A HS configuration is jammed if its reduced pressure $p_{entro} > 10^5$ and the average coordination number (the average number of contacts per particle) z_j satisfies the isostatic condition, $z_j = 2d = 6$. In the calculation of coordination number, we remove the rattlers who have less than four contacts. We stop shear simulations if the system reaches the maximum strain $\gamma_{max} = 0.2$ without jamming. This maximum strain $\gamma_{max} = 0.2$ is greater than the typical yielding strain $\gamma_Y \sim 0.1$ of our model [21].

Now we are ready to explore the J-plane using the thermal protocol. Similar to the athermal case, we apply TC to obtain isotropically jammed packings, and TC+TQS to obtain shear jammed packings, starting from a large number of independent samples of initial states generated at $\{\varphi_{eq}, 0\}$.

B. Minimum isotropic jamming density

The minimum isotropic jamming density $\varphi_{IJ}^{min,th}$ is obtained, in principle, in the limits of $\Gamma \rightarrow \infty$ and $\varphi_{eq} \rightarrow 0$, because $\varphi_{IJ}(\varphi_{eq}, \Gamma)$ decreases with increasing Γ (Fig. 9a) or decreasing φ_{eq} (Fig. 10). However, Fig. 9b shows that the packings generated by the thermal protocol are isostatic, i.e. $z_j = 6$, only when $\Gamma \leq 3 \times 10^{-4}$. Based on that, we determine $\varphi_{IJ}^{min,th} = \varphi_{IJ}(\varphi_{eq} = 0, \Gamma = 3 \times 10^{-4}) = 0.665$ (Table I), which is slightly larger than the J-point density $\varphi_J = 0.655$. We restrict our simulations to small compression rates $\Gamma \leq 3 \times 10^{-4}$, that is, only isostatic packings are considered.

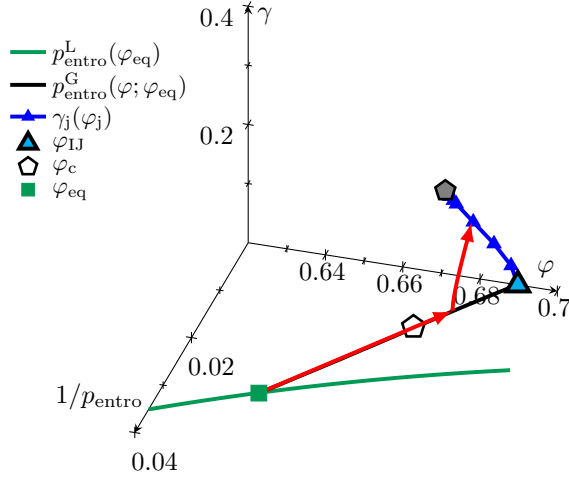


FIG. 8. Illustration of the thermal protocol (to be compared with the athermal protocol, see Fig. 2). The example (red arrow line) shows how a shear jammed packing of $N = 8000$ HSs is obtained. The system is compressed from $\varphi_{\text{eq}} = 0.643$ to the target density $\varphi_j = 0.678$ with a constant compression rate $\Gamma = 10^{-4}$, and then is sheared with a constant shear rate $\dot{\gamma} = 10^{-4}$, which results in shear jamming at strain $\gamma_j = 0.095$.

C. State-following jamming density

Figure 10 shows that, when φ_{eq} is above a certain density $\varphi_{\text{SF}} \approx 0.60$ (Table I), the function $\varphi_{\text{IJ}}(\varphi_{\text{eq}})$ becomes linear and independent of the compression rate Γ . The data obtained from the ARC, which corresponds to the limit of infinitely rapid quench ($\Gamma \rightarrow \infty$), also collapses onto the same linear function for $\varphi_{\text{eq}} > \varphi_{\text{SF}}$. We define the state-following jamming density $\varphi_{\text{J}}^{\text{SF}} = \varphi_{\text{IJ}}(\varphi_{\text{SF}}) \approx 0.67$ (Table I) as the minimum density of isotropically jammed states that can be obtained independent of the compression rate Γ . Above φ_{eq} , the final state after quench can be unambiguously mapped onto the initial state, which is the reason why the quench dynamics are called “state-following” [36]. We point out that, for sufficiently small Γ , activated dynamics will play a role. However, such small Γ cannot be reached in our current simulations, and will not be considered. In Sec. VII, we will discuss the connection between the state-following quench dynamics and the reversibility of jamming under shear.

D. Jamming-line: the thermal case

The J-line Eq. (1), which is here generalized to

$$\varphi_{\text{IJ}} = \varphi_{\text{IJ}}(\varphi_{\text{eq}}, \Gamma), \quad (11)$$

is obtained by varying the compression rate Γ and the initial density φ_{eq} (see Fig. 10). It covers a range of jamming densities, $\varphi_{\text{IJ}}(\varphi_{\text{eq}}, \Gamma) \in [\varphi_{\text{IJ}}^{\text{min,th}}, \varphi_{\text{IJ}}^{\text{max,th}}]$. For a given Γ , the isotropic jamming density φ_{IJ} decreases with decreasing φ_{eq} , and becomes independent of φ_{eq} below

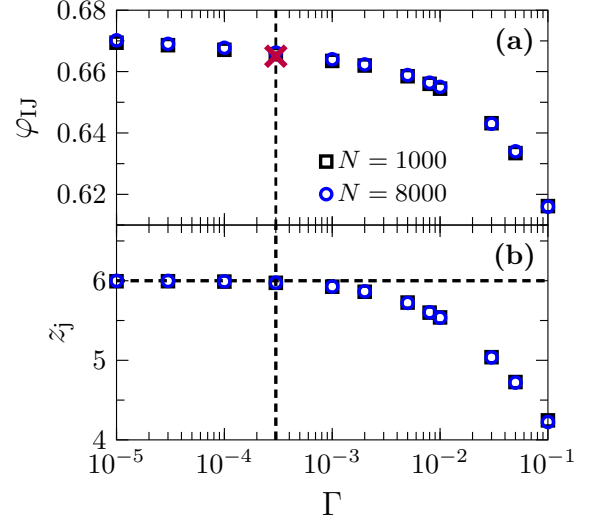


FIG. 9. (a) Isotropic jamming density φ_{IJ} and (b) average coordination number z_j (without rattlers) as functions of compression rate Γ , for $\varphi_{\text{eq}} = 0$ and two different N , obtained by the thermal protocol. The vertical dashed line represents $\Gamma = 3 \times 10^{-4}$, and the cross represents $\varphi_{\text{IJ}}^{\text{min,th}} = 0.665$. No appreciable system-size dependence is observed.

φ_{onset} . The minimum value $\varphi_{\text{IJ}}(\varphi_{\text{eq}} < \varphi_{\text{onset}}, \Gamma)$ itself decreases with increasing Γ , and converges to $\varphi_{\text{IJ}}^{\text{min,th}} = 0.665$ as $\Gamma \rightarrow 3 \times 10^{-4}$ (see also Sec. VIB). The upper bound $\varphi_{\text{IJ}}^{\text{max,th}}$, on the other hand, only depends on $\varphi_{\text{eq}}^{\text{max}}$ as in the athermal protocol, and is independent of Γ . Because $\varphi_{\text{IJ}}^{\text{min,th}} > \varphi_{\text{J}}$, it is impossible to reach the J-point in the thermal protocol. It also means that the thermal protocol explores a narrower part of the J-line compared to the athermal protocol. We have checked that the finite-size effect of φ_{IJ} in the thermal protocol is negligible, see Fig. 9(a) for the case of $\varphi_{\text{eq}} = 0$, and Fig. 12(b) (blue triangles) for the case of $\varphi_{\text{eq}} = 0.643$.

E. Jamming-plane: the thermal case

Different from the athermal case, thermal HSs do not only display the behavior of jamming under constant volume shear. A HS glass quenched from φ_{eq} yields if the shear deformation is applied at $\varphi < \varphi_c(\varphi_{\text{eq}})$, and jams if $\varphi > \varphi_c(\varphi_{\text{eq}})$ [21, 48], see Fig. 11(a). Therefore, shear yielding and shear jamming are separated by the yielding-jamming separation point at φ_c [21]. According to the mean-field theory [48], this point is a critical point, which however is not the case in finite dimensions [21]. In Fig. 11(b), we plot $\varphi_c(\varphi_{\text{eq}})$ for a few different φ_{eq} on the HS phase diagram, which is qualitatively consistent with the mean-field result [49]. To avoid confusion we note that Fig. 11(a) shows the *entropic* stress-strain curve of thermal HSs, which must be distinguished from the *mechanical* stress-strain curve of athermal SSs. Athermal yielding of SSs happens above jamming $\gamma > \gamma_j$.

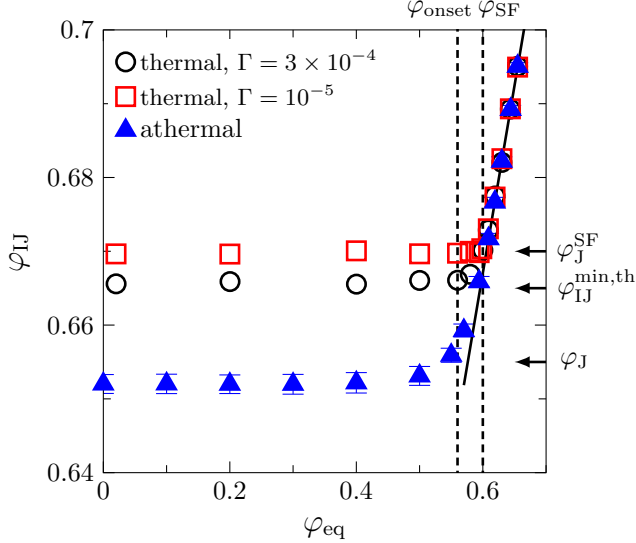


FIG. 10. Isotropic jamming density φ_{IJ} as a function of φ_{eq} , for $N = 1000$ and two different compression rates Γ , obtained by the thermal protocol (compare with Fig. 5 for the athermal case). The $N = 1000$ athermal data from Fig. 5 is also plotted. The vertical lines mark $\varphi_{onset} \approx 0.56$ and $\varphi_{SF} \approx 0.60$. The horizontal arrows mark jamming densities $\varphi_J = 0.655(1)$, $\varphi_{IJ}^{min,th} = 0.665$, and $\varphi_J^{SF} \approx 0.67$. The solid line represents the function $\varphi_{IJ}(\varphi_{eq}) = 0.51\varphi_{eq} + 0.36$ obtained from linear fitting to the data in the regime $\varphi_{eq} \geq \varphi_{SF}$.

We next perform a finite-size analysis of thermal shear jamming. We denote the fraction of shear jamming by $f_c(\varphi_j, N, \varphi_{eq})$ (and therefore $1 - f_c(\varphi_j, N, \varphi_{eq})$ is the fraction of shear yielding) and by $\gamma_j(\varphi_j, N, \varphi_{eq})$ the average jamming strain. As an example, we fit the data of $f_c(\varphi_j, N, \varphi_{eq} = 0.643)$ to the form (see Fig. 12(a)),

$$f_c(\varphi_j, N, \varphi_{eq}) = \frac{1}{2} + \frac{1}{2} \text{erf} \{ [\varphi_j - \varphi_c(N, \varphi_{eq})] / w_c(N, \varphi_{eq}) \}. \quad (12)$$

We then estimate the values of the asymptotic density $\varphi_c^\infty(\varphi_{eq})$, the exponents μ_c and ω_c (see Table II) using the finite-size scaling forms (see Fig. 12(b), Fig. 4(c) and (f)),

$$\varphi_c(N, \varphi_{eq}) = \varphi_c^\infty(\varphi_{eq}) - aN^{-\mu_c}, \quad (13)$$

and

$$w_c(N, \varphi_{eq}) = bN^{-\omega_c}. \quad (14)$$

The data in Table II show that $\varphi_{SJ}^\infty < \varphi_c^\infty < \varphi_{IJ}^\infty$. The exponents of μ , for both athermal and thermal cases, are universal within the numerical accuracy, $\mu_{IJ} \approx \mu_{SJ} \approx \mu_c \approx 0.5$, while ω_c is clearly smaller than 0.5. The SJ-lines Eq. (2), obtained by the thermal protocol, have negligible finite-size effects (Fig. 12(c)). To represent the J-plane, in Fig. 13 we plot the SJ-lines for a few different φ_{eq} obtained by the thermal protocol.

We compare the J-plane obtained by the athermal (see Fig. 7) and the thermal (see Fig. 13) protocols in

Fig. 14(a). The SJ-lines obtained by the two protocols match, but the thermal protocol explores a smaller region of the J-plane than the athermal protocol. We explain in Sec. VII the reason for this difference.

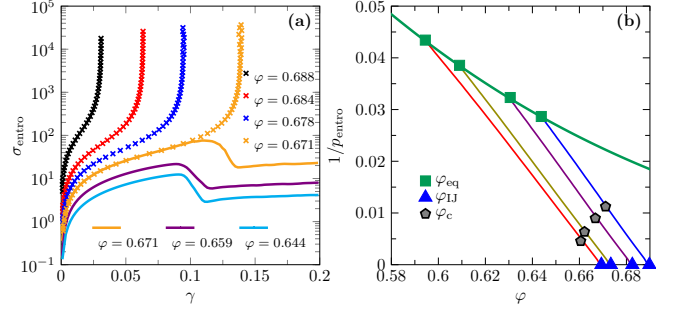


FIG. 11. Shear yielding and shear jamming in thermal HSs. (a) Entropic stress-strain curves at a few different φ , for $\varphi_{eq} = 0.643$ and $N = 8000$. (b) Yielding-jamming separation points $\varphi_c(\varphi_{eq})$ on the $1/p_{entro} - \varphi$ phase diagram. The green line represents the liquid EOS $p_{entro}^L(\varphi_{eq})$, and the other lines represent the glass EOSs $p_{entro}^G(\varphi; \varphi_{eq})$ for $\varphi_{eq} = 0.595, 0.609, 0.630, 0.643$ (from left to right).

VII. REVERSIBILITY

In previous sections, we discussed how to reach jamming at $\{\varphi_j, \gamma_j\}$ starting from HS liquid states at $\{\varphi_{eq}, 0\}$, using either athermal or thermal protocols. Here we ask whether such routes to jamming can be reversed. We point out that the reversibility mainly depends on the state variables φ_j and γ_j , with an intrinsic relationship to φ_{eq} , rather than on the protocol itself (athermal or thermal). The difference between athermal and thermal protocols lies in the accessibility to irreversible-jamming. In the following, we will focus on using the athermal protocols (ARC and AQS) to examine the reversibility. In [21], we have found that the routes to shear jamming are reversible under TQS, for the few cases studied, which have $\varphi_{eq} > \varphi_{SF}$ and $\varphi_j > \varphi_c(\varphi_{eq})$. That observation is consistent with the systematic study presented below using the athermal protocols.

A. Definition

In Sec. V, we described how to use the athermal protocol to generate a jammed configuration at $\{\varphi_j, \gamma_j(\varphi_j; \varphi_{eq})\}$, from the initial equilibrium state at $\{\varphi_{eq}, 0\}$. The procedure consists of two steps,

$$\text{ARC : } \{\varphi_{eq}, 0\} \rightarrow \{\varphi_j, 0\}, \quad (15)$$

$$\text{AQS : } \{\varphi_j, 0\} \rightarrow \{\varphi_j, \gamma_j(\varphi_j; \varphi_{eq})\}. \quad (16)$$

Let us recall that a fraction of f_{IJ} samples jam at $\{\varphi_j, 0\}$ simply by the ARC procedure (Eq. (15)) without adding

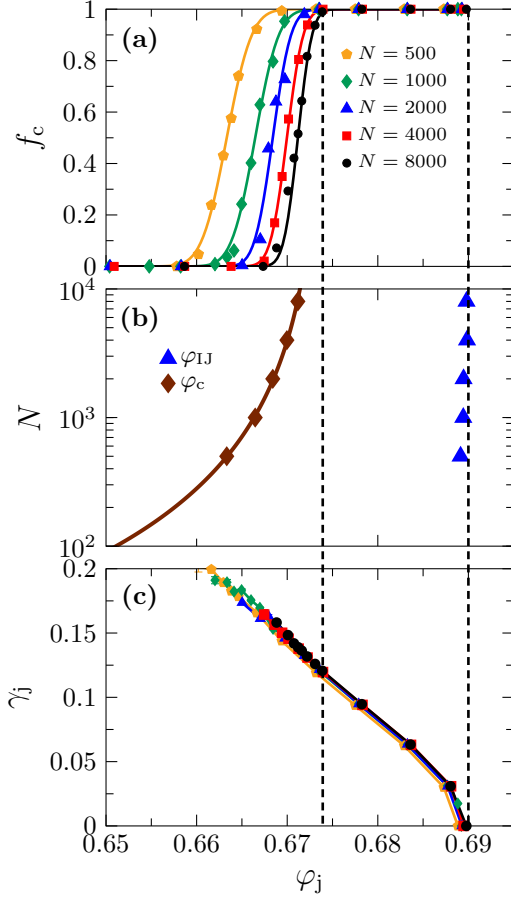


FIG. 12. System-size dependence of jamming in the thermal protocol for $\varphi_{eq} = 0.643$ (compare with Fig. 3 for the athermal case). (a) Fraction f_c of shear jamming as a function of φ_j , for a few different N . The data points are fitted to Eq. (12) (lines). (b) The data of $\varphi_c(N)$ is fitted to Eq. (13), see Fig. 4(c) for the log-log plot. We do not attempt to fit $\varphi_{IJ}(N)$ to any scaling forms, since the N -dependence is negligible (see also Fig. 9(a)). The asymptotic densities (see Table II), $\varphi_c^\infty = 0.674(1)$, and $\varphi_{IJ}^\infty = 0.690(1)$ that is obtained by the athermal protocol for the same φ_{eq} , are marked by vertical dashed lines. (c) The shear jamming strain γ_j is plotted as a function of φ_j for a few different N , which shows that the system size dependence is negligible.

shear. For the rest of unjammed samples, we further apply AQS (Eq. (16)) to shear jam them at $\{\varphi_j, \gamma_j(\varphi_j; \varphi_{eq})\}$. Therefore, in principle we can study the reversibility of the two steps, compression jamming and shear jamming, separately. It turns out that each reversible-jamming state, either compression or shear jammed, is uniquely associated with a metastable glass basin quenched from $\{\varphi_{eq}, 0\}$.

To quantify the reversibility, we apply a single cycle of compression or shear, and measure the relative mean square displacement (RMSD) $\Delta_r = \frac{1}{N} \sum_{i=1}^N |\mathbf{r}_i^{\text{after}} - \mathbf{r}_i^{\text{before}}|^2$ between the configuration $\{\mathbf{r}_i^{\text{before}}\}$ before the cycle and the configuration $\{\mathbf{r}_i^{\text{after}}\}$

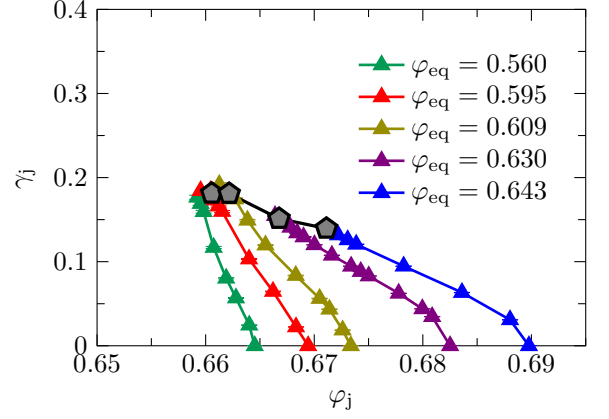


FIG. 13. J-plane obtained by the thermal protocol, represented by typical SJ-lines $\gamma_j(\varphi_j; \varphi_{eq})$ for a few different φ_{eq} ($N = 8000$). These SJ-lines are bounded from above by the yielding-jamming separation line $\{\varphi_c(\varphi_{eq}), \gamma_c(\varphi_{eq})\}$ (pentagons), where $\gamma_c(\varphi_{eq}) = \gamma_j(\varphi_j = \varphi_c; \varphi_{eq})$. Compare with Fig. 7 for the athermal case.

after. We use a threshold value $\Delta_{th} = 0.025$, which is about the average cage size of particles in the glass states at φ_d [44]: if $\Delta_r < \Delta_{th}$, the route to the jammed state belongs to *reversible-jamming*; otherwise *irreversible-jamming*.

Note that $\{\mathbf{r}_i^{\text{before}}\}$ and $\{\mathbf{r}_i^{\text{after}}\}$ are both unjammed configurations. We are interested in whether $\{\mathbf{r}_i^{\text{before}}\}$ and $\{\mathbf{r}_i^{\text{after}}\}$ are similar enough such that they belong to the same glass state. The reversible-jamming means that, during the route to jamming, the system remains in the same meta-stable glass basin. Our definition of reversibility shall be distinguished from the one used in some previous studies [16, 50, 51], where a jammed state is called reversible under cyclic AQS only if all particles return to the exactly same positions at jamming. The present definition is essentially the same as the one employed in [21] for TQS in thermal HSs.

B. Reversible-jamming and irreversible-jamming

First let us study the reversibility of the ARC jamming procedure (Eq. (15)). In Sec. V, we have shown that there is a mapping between the isotropic jamming density φ_{IJ} and φ_{eq} , described by Eq. (1) (recall that φ_{IJ} is the most probable jamming density φ_j obtained by ARC for the given φ_{eq} , see Eq. (5)). In Fig. 15 (a) we show the RMSD Δ_r measured by one cycle of ARC: $\{\varphi_{eq}, 0\} \rightarrow \{\varphi_j = \varphi_{IJ}, 0\} \rightarrow \{\varphi_{eq}, 0\}$. It can be seen that in the range $\varphi_{eq} > \varphi_{SF} \approx 0.60$, $\Delta_r < \Delta_{th}$ so that ARC is reversible. On the other hand, for $\varphi_{eq} < \varphi_{SF}$, Δ_r becomes much larger Δ_{th} so that ARC is irreversible. Interestingly, the point $\varphi_{eq} = \varphi_{SF}$ that separates reversible-jamming and irreversible-jamming coincides with the one that separates compression rate-independent (i.e., state-following) and compression rate-dependent quench dy-

namics (see Fig. 10). We will interpret this observation in Sec. VII C.

Next we analyze the reversibility of AQS Eq. (16), by considering the fraction $1 - f_{IJ}$ of samples that remain unjammed at φ_j after ARC. We apply one cycle of AQS, $\{\varphi_j, 0\} \rightarrow \{\varphi_j, \gamma_j(\varphi_j; \varphi_{eq})\} \rightarrow \{\varphi_j, 0\}$, and measure the associated RMSD Δ_r . In Fig. 15(b) we show how Δ_r increases with the jamming strain γ_j along SJ-lines Eq. (2). From the data we extrapolate the RMSD at the zero strain limit $\Delta_r^0 = \Delta_r(\gamma_j \rightarrow 0)$ for each SJ-line, and plot it as a function of φ_{eq} (Fig. 15(a)). The data shows that Δ_r^0 grows above Δ_{th} as φ_{eq} decreases below φ_{SF} , which is consistent with the results obtained by ARC.

In Fig. 14(b), we show the heat-map of Δ_r measured by the AQS cycle, which suggests that the J-plane can be divided into two parts: reversible-jamming and irreversible-jamming. Comparing Fig. 14(a) and (b), we find that the reversible-jamming part corresponds to the domain that can be accessed by the thermal protocols (TC/TQS) with $\varphi_{eq} > \varphi_{SF}$. Therefore, most of the packings generated by the thermal protocol are reversible, while those generated by the athermal protocols (ARC/AQS) can be both reversible and irreversible. Note that the packings in the reversible-jamming regime are reversible in both thermal and athermal protocols. In fact, other properties of the packings in this regime are also independent of the jamming protocol (see Sec. VIII, IX, and X).

Figure 14(b) shows that there are two boundary lines between reversible-jamming and irreversible-jamming: the state-following line, which is the thermal SJ-line obtained from $\varphi_{eq} = \varphi_{SF}$, and the yielding-jamming separation line $\{\varphi_c(\varphi_{eq}), \gamma_c(\varphi_{eq})\}$. They are associated to two different mechanisms respectively, quench dynamics and yielding of HS glasses, as explained in detail below.

C. Connection to quench dynamics

To explain the above observation, we borrow the framework obtained by a recent mean-field theory of spherical *mixed* p-spin model [40, 52] (note the equivalence between the temperature quench in the spin model and the compression quench in our model), which revealed some important features missing in usual *pure* p-spin models.

(i) The reversible-jamming regime corresponds to the state-following dynamical regime that only exists for $\varphi_{eq} > \varphi_{SF}$. A jammed state in this regime is “followed” from, and only depends on, the initial equilibrium state at φ_{eq} . Upon compression or shear jamming, the state remains in the same metastable glass basin, and the memory of the initial condition is kept. Therefore, the route to jamming is reversible (Figs. 14 and 15), and the function $\varphi_{IJ}(\varphi_{eq})$ is independent of protocol parameters such as the compression rate Γ (Fig. 10).

(ii) The irreversible-jamming regime corresponds to the so-called *hic sunt leones* dynamical regime observed

in Ref. [40], which exists for $\varphi_{onset} < \varphi_{eq} < \varphi_{SF}$. Such quench dynamics are rather complicated and not fully understood even in the spin glass models [40, 52]. Upon compression or shear jamming, the memory of the initial condition is partially lost, and the final state is protocol-dependent.

(iii) The SJ-line, $\gamma_j = \gamma_j(\varphi_j = \varphi_J, \varphi_{eq} < \varphi_{onset})$, which is vertical in the thermodynamical limit and is the leftmost boundary of the J-plane, corresponds to the memory-less dynamical regime for $\varphi_{eq} < \varphi_{onset}$. The jamming density after quench is always φ_J , which is completely independent of the initial condition.

Based on the above analogy, we attribute the irreversible-jamming for $\varphi_{eq} < \varphi_{SF}$ to the loss or the partial loss of memory during quench. This mechanism determines one boundary between reversible-jamming and irreversible-jamming, i.e., the state-following line.

D. Connection to yielding of hard sphere glasses

In Fig. 16 (a), we plot RMSD Δ_r as a function of φ_j along the SJ-line Eq. (3), for $\varphi_{eq} = 0.643$. The reversible-jamming ($\Delta_r < \Delta_{th}$) and irreversible-jamming ($\Delta_r > \Delta_{th}$) parts are separated by $\varphi_c(\varphi_{eq} = 0.643) = 0.671$, which is also the density separates shear yielding and shear jamming in thermal HSs (see Fig. 11 and Sec. VI E).

To understand the reason for the irreversibility when $\varphi_j < \varphi_c$, we analyze how Δ_r increases along the route to shear jamming. We first use ARC to compress the system from $\varphi_{eq} = 0.643$ to $\varphi = 0.6555$ (φ is chosen below φ_c), and then apply a cycle of AQS, $\{\varphi, 0\} \rightarrow \{\varphi, \gamma\} \rightarrow \{\varphi, 0\}$, at the fixed density $\varphi = 0.6555$. In Fig. 16 (d) we plot Δ_r as a function of increasing strain γ . Note that, for $\gamma < \gamma_j(\varphi = 0.6555, \varphi_{eq} = 0.643) = 0.36$, the configuration is not jammed during the cycle of shear. The data shows that Δ_r increases with γ and becomes significantly larger than Δ_{th} as $\gamma \rightarrow \gamma_j$. However, Δ_r is nearly zero below the yielding strain $\gamma_Y(\varphi = 0.6555, \varphi_{eq} = 0.643) \approx 0.1$ of HS glasses, which suggests that the onset of irreversible-jamming might be related to the yielding of HS glasses.

Considering that Δ_r is measured in the athermal protocol, the above observation is rather surprising at first glance: why would the behavior of an unjammed athermal system, which is sometimes considered as a “liquid” (because $P_{mech} = \Sigma_{mech} = 0$) [4], has anything to do with yielding that typically only occurs in solids? To further reveal the connection, we measure entropic stress-strain curves of unjammed configurations obtained by the two different protocols: we use ARC to compress the system from $\varphi_{eq} = 0.643$ to $\varphi = 0.6555$, shear it using AQS (with SS potential) or TQS (with HS potential) up to a strain γ , and then measure its entropic stress σ_{entro} by switching on the temperature (with HS potential). Note that as long as $\gamma < \gamma_j$, the athermal SS configurations are unjammed, which allows us to switch to the HS potential because there is no overlapping between the particles. Figure 16(c) shows that the entropic stress-strain curves

of athermal and thermal configurations coincide below γ_Y . The bifurcation occurs around γ_Y : the entropic stress σ_{entro} of the athermal system tends to diverges as $\gamma \rightarrow \gamma_j$, while that of the thermal system reaches a plateau after yielding, $\gamma > \gamma_Y$.

These surprising results suggest that, these athermal configurations, even though unjammed, should be understood as glass states rather than liquid states. After yielding, the system leaves the metastable glass basin and explores a larger configurational space [34]. The athermal protocol stops only when it successfully finds a jammed configuration that belongs to a different glass basin, and therefore the route is not reversible. In the thermal protocol, the thermal activations can overcome free-energy barriers between different glass basins. After yielding, the system eventually reaches a stationary flow instead of jamming. Note that one can also interpret yielding as the end point of state-following dynamics under shear [35], which is consistent with the mechanism discussed in Sec. VII C.

We finally make a comparison between the J-plane and the stability-reversibility map of HS glasses obtained in Ref. [21] (Fig. 16(b)). The HS stability-reversibility map describes stability and reversibility of thermal HS glasses under volume and shear strains. In the *reversible-glass* (stable glass) regime, the glass responds elastically to shear. In the *partially irreversible-glass* (marginally stable glass) regime, the glass is marginally stable and experiences mesoscopic plastic deformations under shear. At larger strains, the system either yields and becomes irreversible, or jams. To avoid confusion, we use reversible-glass/irreversible-glass/partially irreversible-glass for the stability-reversibility map, and reversible-jamming/irreversible-jamming for the J-plane. The irreversible-jamming part of the SJ-line lies in the irreversible-glass regime, as a consequence of HS yielding detected by the measurement of the entropic stress discussed above. The reversible-jamming part of the SJ-line belongs to the partially irreversible-glass regime, because the system remains in the same meta-stable glass state despite of the plasticity (see Fig. 1 of Ref. [21] and the discussion there).

VIII. ISOSTATICITY AND JAMMING UNIVERSALITY

In this section we show that all packings on the J-plane, either compression jammed or shear jammed, are isostatic, and belong to the same universality jamming class.

First, we show that the coordination number at the jamming/unjamming transition satisfies the isostatic condition. We compress the SS packings athermally from $\{\varphi_j, \gamma_j\}$ to $\{\varphi > \varphi_j, \gamma_j\}$, keeping the shear strain γ_j unchanged. We then measure the coordination number z (without rattlers) as a function of φ . Figure 17(a) shows that the coordination number z satisfies the isostatic con-

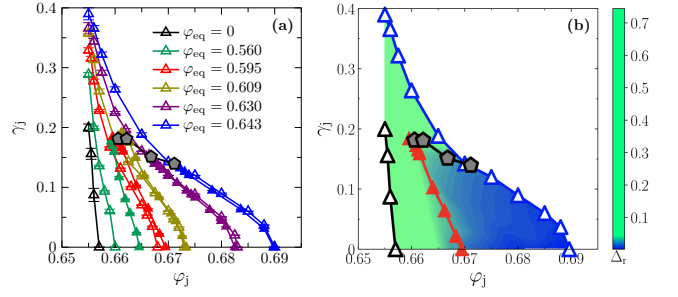


FIG. 14. Reversible-jamming and irreversible-jamming. (a) Numerical data of the SJ-lines, for $N = 8000$ and a few different φ_{eq} (same data as in Figs. 7 and 13). The filled and open symbols correspond to thermal and athermal protocols, respectively. (b) J-plane colored according to the RMSD Δ_r measured by one cycle of AQS (see text for details). The reversible-jamming (blue) and the irreversible-jamming (green) regimes are separated by the yielding-jamming separation line (pentagon line), and the state-following line corresponding to the thermal SJ-line for $\varphi_{\text{eq}} = \varphi_{\text{SF}}$ (red filled triangle line).

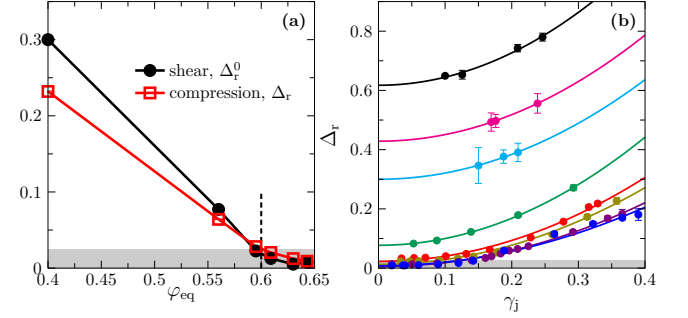


FIG. 15. The RMSD measured by one cycle of ARC or AQS. (a) The RMSD Δ_r of an ARC-cycle, and the zero strain RMSD Δ_r^0 of an AQS-cycle (obtained from (b)), are plotted as functions of φ_{eq} . The location of $\varphi_{\text{SF}} \approx 0.60$ is indicated by the vertical dashed bar. The RMSD is smaller than $\Delta_{\text{th}} = 0.025$ in the shaded region. (b) RMSD Δ_r of an AQS-cycle as a function of the jamming strain γ_j , along SJ-lines for $N = 8000$ and a few different φ_{eq} (from top to bottom, $\varphi_{\text{eq}} = 0, 0.2, 0.4, 0.56, 0.595, 0.609, 0.630, 0.643$). The data points are fitted to an empirical form $\Delta_r(\gamma_j) = \Delta_r^0 + c\gamma_j^2$ (lines). The zero strain RMSD Δ_r^0 is plotted as a function of φ_{eq} in (a).

dition $z = z_j = 6$, at the unjamming transition where $e_{\text{mech}} \rightarrow 0$ from above jamming. Consistently, Fig. 17(c) shows that the isostatic condition also holds at the jamming transition where $p_{\text{entro}} \rightarrow \infty$ from below jamming in thermal HSs. Moreover, the isostatic condition is valid for any packing along the SJ-line, independent of γ_j (Fig. 17(a) and (c)).

Second, we show that all packings above jamming ($\varphi > \varphi_j$) follow the same set of scaling laws. Under athermal compressions, the pressure P_{mech} , the energy E_{mech} and the coordination number z all increase in SS packings. Figure 17(a) shows that, for packings along the SJ-line with the same $\varphi_{\text{eq}} = 0.643$ but different φ_j (blue triangle

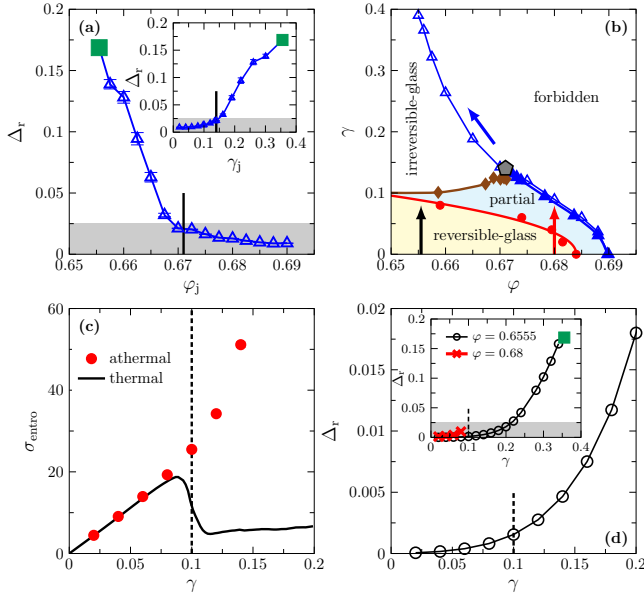


FIG. 16. Connection between irreversible-jamming and HS yielding. Data are obtained for $\phi_{eq} = 0.643$ and $N = 8000$, and the AQS-cycle is used to measure Δ_r . (a) RMSD Δ_r as a function of ϕ_j and (inset) γ_j along the SJ-line. The vertical bars represent $\phi_c(\phi_{eq} = 0.643) = 0.671$, and (inset) $\gamma_c(\phi_{eq} = 0.643) = 0.14$. The shaded area represents the region with $\Delta_r \leq \Delta_{th}$. (b) Stability-reversibility map of HS glasses (adapted from Ref. [21]). The brown diamonds and red circles represent the HS yielding line and the Gardner line. The open and filled triangles are the same SJ-line data as in Fig. 14(a). (c) Entropic stress σ_{entro} of unjammed configurations obtained from both athermal and thermal protocols, as functions of γ , for a fixed $\phi = 0.6555 < \phi_c$ (black arrow in (b)). (d) RMSD Δ_r as a function of γ for $\phi = 0.6555$. The inset shows the data in a larger range of γ , as well as the data for $\phi = 0.68 > \phi_c$ (red arrow in (b)). The vertical dashed lines in (c) and (d) represent the thermal HS yielding strain $\gamma_Y(\phi = 0.6555, \phi_{eq} = 0.643) \approx 0.1$. The green squares in (a) and (d) represent the same point at $\{\phi_j = 0.6555, \gamma_j = 0.36\}$.

line in Fig. 7), the data of energy density e_{mech} versus z collapse onto the same master curve, which vanishes at $z_j = 6$. Furthermore, the following scalings, which are well known for isotropically jammed packings [4], are also satisfied in shear jammed packings (Fig. 17b),

$$P_{mech} \sim \phi - \phi_j, \quad (17)$$

and

$$z - z_j = (\phi - \phi_j)^{1/2}. \quad (18)$$

Third, we examine the scaling behavior below jamming ($\phi < \phi_j$). To do that, we compute the cumulative structure function $Z(r)$ of HS packings along the SJ-line for $\phi_{eq} = 0.643$. The packings are compressed or sheared until the pressure reaches $p_{entro} = 10^{12}$. The cumulative structure function is defined as

$$Z(r) = \rho \int_0^r ds 4\pi s^2 g(s), \quad (19)$$

where $g(s)$ is the pair correlation function,

$$g(s) = \frac{1}{4\pi s^2 \rho N} \left\langle \sum_{i \neq j} \delta(s - r_{ij}/D_{12}) \right\rangle, \quad (20)$$

with $\delta(x)$ being the delta function. The cumulative structure function $Z(r)$ exhibits a plateau at $z_j = 6$ (Fig. 17c). The growth from this plateau satisfies the scaling

$$Z(r) - z_j \sim (r - 1)^{1-\alpha}, \quad (21)$$

where $\alpha = 0.41269$ [23]. This scaling is predicted by the mean-field theory and has been verified numerically for isotropically jammed packings in finite dimensions [23]. Here we show that it also holds for shear jammed packings.

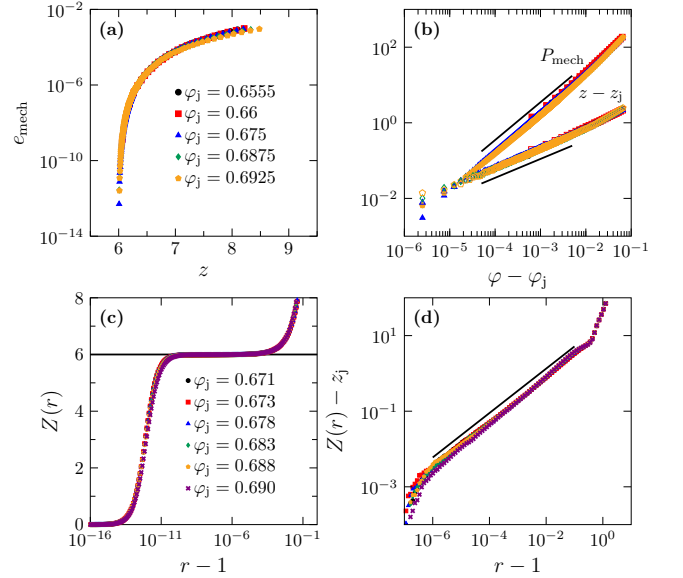


FIG. 17. Isostaticity and universality of jamming. We show scalings (a-b) above jamming $\phi > \phi_j$ in athermal SSs, and (c-d) below jamming $\phi < \phi_j$ in thermal HSs, for $\phi_{eq} = 0.643$ and $N = 8000$. Data in (a-b) are obtained from athermal compressions of SS packings from ϕ_j to ϕ , for a few different ϕ_j along the SJ-line (blue triangle line in Figs. 7 and 14). (a) Energy density e_{mech} versus coordination number z . (b) Pressure P_{mech} and the excess coordination number $z - z_j$ as functions of $\phi - \phi_j$. The data are consistent with scalings Eqs. (17) and (18) (lines). (c) Cumulative structure function $Z(r)$ of HSs below jamming, for a few different ϕ_j along the SJ-line (blue triangle line in Figs. 13 and 14). The black line indicates the isostatic coordination number $z_j = 6$. (d) The data of $Z(r)$ is consistent with the critical jamming scaling Eq. (21) (line).

IX. ANISOTROPY

We use the anisotropy parameter R_A , which is based on the fabric tensor \hat{R} , to quantify the anisotropy of contact networks in jammed packings. The fabric tensor is

defined as

$$\hat{R} = \frac{1}{N} \sum_{i \neq j} \frac{\mathbf{r}_{ij}}{|\mathbf{r}_{ij}|} \otimes \frac{\mathbf{r}_{ij}}{|\mathbf{r}_{ij}|}, \quad (22)$$

where \mathbf{r}_{ij} is the vector connecting two particles i and j that are in contact, and \otimes denotes a vector outer product. The eigenvalues of \hat{R} are denoted by λ_1 , λ_2 and λ_3 , and the coordination number is related to the eigenvalues by $z_j = \lambda_1 + \lambda_2 + \lambda_3$. The fabric anisotropy parameter R_A is defined as the difference between the largest and the smallest eigenvalues, normalized by z_j , $R_A = (\lambda_{\max} - \lambda_{\min})/z_j$ [13].

Another important quantity to characterize the anisotropy is the contact angle probability distribution $P_\theta(\theta)$, where the angle θ is defined through the coordinate transformation $\mathbf{r}_{ij} = (r_{ij} \sin \theta \sin \phi, r_{ij} \cos \phi, r_{ij} \cos \theta \sin \phi)$, considering that the shear strain is applied in the $x - z$ plane. From the lowest order Fourier expansion, $P_\theta(\theta)$ is related to the fabric anisotropy parameter R_A via [24],

$$P_\theta(\theta) \approx \frac{1}{2\pi} [1 + 2R_A \cos 2(\theta - \theta_c)], \quad (23)$$

where θ_c is the principle direction.

Apparently, for isotropic jamming ($\gamma_j = 0$), the fabric anisotropy parameter R_A should be nearly zero, and the contact angle distribution should be uniform, as confirmed in Figs. 18(a) and (c). For shear jamming, let us consider two cases. In the case $\varphi_{\text{eq}} = 0$, the fabric anisotropy parameter immediately jumps to a finite value $R_A \approx 0.03$ for non-zero γ_j , and stays as a constant for larger γ_j (Fig. 18a and b), which is consistent with the observation in [53] (Ref. [53] also suggests that $R_A(\gamma_j)$ would jump discontinuously at $\gamma_j = 0$ in the thermodynamic limit). Accordingly, the contact angle distribution $P_\theta(\theta)$, with $\theta_c = 135^\circ$, also quickly converges to the asymptotic distribution (Fig. 18c). In the case $\varphi_{\text{eq}} = 0.643$, which is above φ_{onset} , the fabric anisotropy does not change monotonically with γ_j (Fig. 18a and b). At intermediate γ_j , the $P_\theta(\theta)$ has a dumbbell shape, indicating a strong anisotropy (Fig. 18d). At larger γ_j , both R_A and $P_\theta(\theta)$ converge to the same asymptotic behaviors as in the case of $\varphi_{\text{eq}} = 0$.

X. BOND-ORIENTATIONAL ORDER

Although the crystalline order is absent in our polydisperse model, the packings could have structures at the local scale [9]. We characterize such order by using the weighted bond-orientational order parameter [54], defined as

$$Q_{l,i}^w = \sqrt{\frac{4\pi}{2l+1} \sum_{m=-l}^l \left| \sum_{j=1}^{n_b(i)} \frac{A_{ij}}{A_i} Y_{l,m}(\mathbf{r}_{ij}) \right|^2}, \quad (24)$$

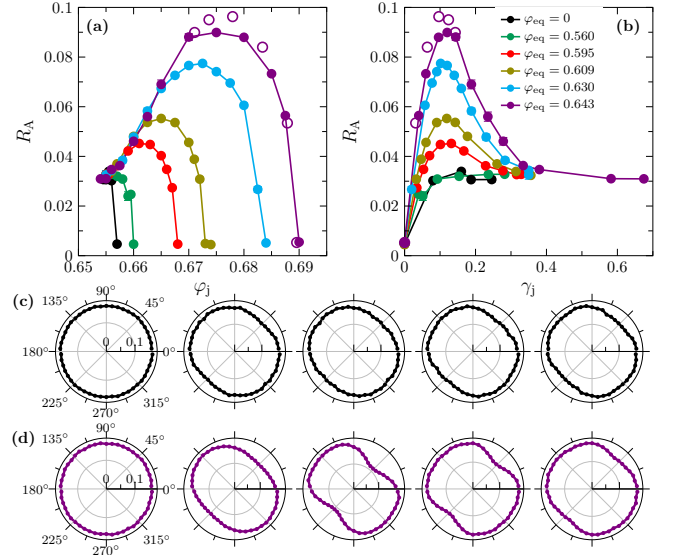


FIG. 18. Contact anisotropy. Fabric anisotropy parameter R_A of packings along SJ-lines, as a function of (a) jamming density φ_j and (b) jamming strain γ_j . Data are obtained for $N = 8000$ and a few different φ_{eq} , by using the athermal protocol (filled symbols) and the thermal protocol (open symbols). (c) Contact angle probability distribution $P_\theta(\theta)$ for $\varphi_{\text{eq}} = 0$ and $\gamma_j = 0, 0.08, 0.16, 0.19, 0.25$ (from left to right). (d) Contact angle probability distribution $P_\theta(\theta)$ for $\varphi_{\text{eq}} = 0.643$ and $\gamma_j = 0, 0.04, 0.12, 0.28, 0.37$ (from left to right).

where $Y_{l,m}(\mathbf{r}_{ij})$ is the spherical harmonic of degree l and order m , A_{ij} is the area of the Voronoi cell face between particles i and j , and $A_i = \sum_j A_{ij}$. Here we consider the average bond-orientational order parameter with $l = 6$:

$$Q_6^w = \frac{1}{N} \sum_i Q_{6,i}^w. \quad (25)$$

Figure 19a shows the $Q_6^w - \varphi_j$ order map [3] obtained from the packings associated to the J-plane. The order parameter Q_6^w of isotropically jammed packings ($\gamma_j = 0$) increases with φ_{eq} . Ref. [43] has shown that this increase is inherited from the initial equilibrium configurations at φ_{eq} . Along SJ-lines, the Q_6^w decreases with decreasing φ_j , or increasing γ_j (Fig. 19b). Interestingly, our result shows that the J-point has the minimum order Q_6^w , and therefore the maximum randomness, among all state points on the J-plane. In this sense, the J-point coincides with the MRJ point introduced in Ref. [3]. However, we emphasize that the crystalline order is excluded from our consideration, which is an essential difference from Ref. [3].

XI. SHEAR JAMMING OF FACE-CENTERED CUBIC CRYSTALS

In order to understand the differences in shear jamming between amorphous and ordered states, we simulate

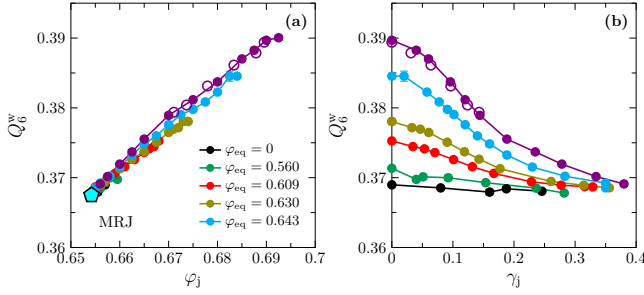


FIG. 19. Order map. The weighted bond-orientational order parameter Q_6^w is plotted as a function of (a) φ_j and (b) γ_j , along SJ-lines with different φ_{eq} .

FCC crystals consisting of $N = 500$ particles. Similar to the amorphous case, crystalline configurations jam under thermal or athermal shear. However, because crystals are in equilibrium, their states are independent of protocol parameters such as φ_{eq} and Γ . As a consequence, the J-plane shrinks to a single SJ-line, whose end point is the state point of the FCC close packing at $\{\varphi_j^{FCC} \simeq 0.74, \gamma_j = 0\}$ (Fig. 20a). Near this point, the SJ-line Eq. (2) follows a simple relationship, $(1 - 2\gamma_j)^2 + 1 = 4(D/l_a)^2$, where l_a is the lattice constant of the unit cell, and $D/l_a = (3\varphi_j/2\pi)^{1/3}$. This relationship is derived from an affine transformation.

In the thermal protocol, the FCC crystals also exhibit shear jamming and yielding, which are separated by the density $\varphi_c \approx 0.69$ (Fig. 20b). In the shear jamming case ($\varphi > \varphi_c$), the stress-strain curve has a small tip before the divergence of the stress σ_{entro} , which indicates the onset of non-affine arrangement. We interpret the tip as a vestige of yielding. The MRS Δ_r increases rapidly below φ_c (Fig. 20c), which suggests that reversible-jamming and irreversible-jamming are separated by φ_c , consistent with the amorphous case.

XII. DISCUSSION

In this paper, the concept of J-plane (Fig. 1) is introduced, and is realized numerically using athermal and thermal protocols. Thanks to the swap algorithm, we are able to explore the J-plane over a wide range of jamming densities. It is possible to replace the role of the swap algorithm by other protocols that are easier to be reproduced in experiments, such as athermal cyclic shear [16] or athermal cyclic compressions [15]. Indeed, similar SJ-lines as in Fig. 7 have been obtained in Ref. [15] (Fig. 6b), although within a much narrower range of densities. We

therefore expect the J-plane to be reproducible in tapping and shear experiments of granular matter.

Our analysis reveals that the J-point is a rather special point on the J-plane. The state at the J-point has the minimum packing density and the maximum randomness among all possible amorphous, frictionless, jammed states. The remaining challenge to theories is to provide a first-principle understanding of the J-point. Our results show that $\varphi_J \neq \varphi_{IJ}(\varphi_{eq} = \varphi_d)$, which rule out the possibility that the state at the J-point is followed from the equilibrium state at the dynamical glass transition density φ_d . Instead, the recent spin-glass theory of quench dynamics [55], together with earlier numerical studies [8], suggest that $\varphi_J = \varphi_{IJ}(\varphi_{eq} \leq \varphi_{onset})$. Therefore generalization of the calculation in Ref. [55] to sphere systems would be very appealing.

We show that the phase space of jammed states can be significantly extended by adding shear, which introduces anisotropy to the contact networks. Our results disapprove the earlier understanding that shear jamming and isotropic jamming always occur at the same jamming density in the thermodynamical limit [18, 19]. The reversibility of the routes to jamming has a deep connection to the reversibility of the corresponding thermal HS glasses upon quench or shear [21].

Finally, we expect our results to pave the way for a set of novel studies. Related open questions include, but are not limited to: do the jammed states on the J-plane share the same rheological properties, before and after yielding [21, 41]? How to extend the J-plane in order to integrate the effects of friction [12, 13, 56] and crystalline order [57]? Can we make a connection between reversible-jamming/irreversible-jamming discussed here and the reversible-irreversible transition in suspensions [58] and granular systems [16, 59]?

ACKNOWLEDGMENTS

This work was supported by KAKENHI (No. 25103005 “Fluctuation & Structure” and No. 19H01812) from MEXT, Japan. Y.J. acknowledges funding from Project 11974361, Project 11935002, and Project 11947302 supported by NSFC, from Key Research Program of Frontier Sciences, CAS, Grant NO. ZDBS-LY-7017, and from the CAS Pioneer Hundred Talents Program. The computations were performed using the computing facilities in Research Center for Computational Science, Okazaki, Japan, the computing facilities in the Cybermedia center, Osaka University, the HPC Cluster of ITP-CAS, and Tianhe-2 Supercomputer, National Supercomputer Center in Guangzhou.

[1] Thomas Hales, Mark Adams, Gertrud Bauer, Tat Dat Dang, John Harrison, Hoang Le Truong, Cezary

Kaliszyk, Victor Magron, Sean McLaughlin, Tat Thang

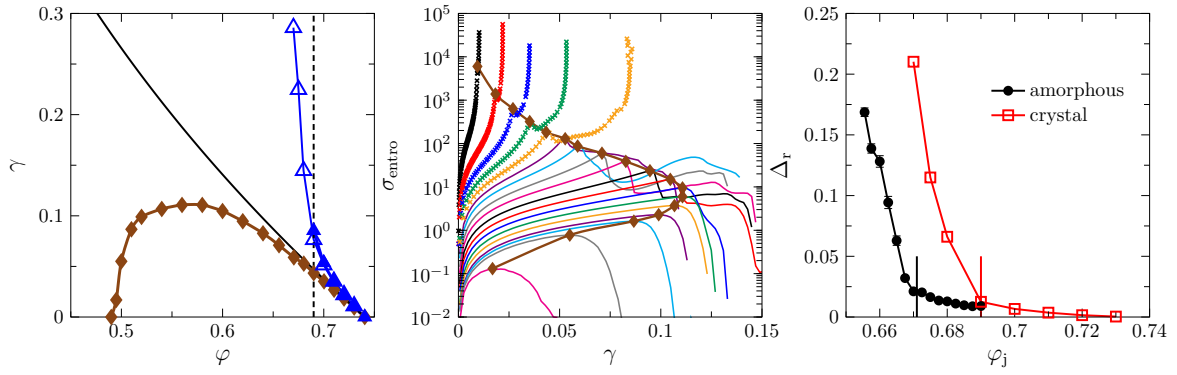


FIG. 20. Shear jamming of FCC crystals ($N = 500$). (a) SJ-lines obtained by the thermal (filled triangles) and the athermal (open triangles) protocols (to be compared with Fig. 16(b)). We also plot the affine law (solid line), the thermal yielding line (diamonds), and $\varphi_c \approx 0.69$ (vertical dashed line) estimated from the data in (b). (b) Stress-strain curves for a few different densities (from bottom to top, $\varphi = 0.495, 0.50, 0.51, 0.52, 0.54, 0.56, 0.58, 0.60, 0.62, 0.64, 0.655, 0.67, 0.68, 0.69, 0.70, 0.71, 0.72, 0.73$). (c) RMSD Δ_r as a function of φ_j for FCC packings, and for amorphous packings with $\varphi_{eq} = 0.643$ (same data as in Fig. 16a). The vertical bars indicate φ_c .

- Nguyen, *et al.*, “A formal proof of the kepler conjecture,” in *Forum of Mathematics, Pi*, Vol. 5 (Cambridge University Press, 2017).
- [2] JD Bernal and J. Mason, “Packing of spheres: coordination of randomly packed spheres,” *Nature* **188**, 910 (1960).
- [3] Salvatore Torquato, Thomas M Truskett, and Pablo G Debenedetti, “Is random close packing of spheres well defined?” *Physical review letters* **84**, 2064 (2000).
- [4] Corey S O’hern, Leonardo E Silbert, Andrea J Liu, and Sidney R Nagel, “Jamming at zero temperature and zero applied stress: The epitome of disorder,” *Physical Review E* **68**, 011306 (2003).
- [5] Andrea J Liu and Sidney R Nagel, “Nonlinear dynamics: Jamming is not just cool any more,” *Nature* **396**, 21 (1998).
- [6] Giorgio Parisi and Francesco Zamponi, “Mean-field theory of hard sphere glasses and jamming,” *Reviews of Modern Physics* **82**, 789 (2010).
- [7] Pinaki Chaudhuri, Ludovic Berthier, and Srikanth Sastry, “Jamming transitions in amorphous packings of frictionless spheres occur over a continuous range of volume fractions,” *Physical review letters* **104**, 165701 (2010).
- [8] Misaki Ozawa, Takeshi Kuroiwa, Atsushi Ikeda, and Kunimasa Miyazaki, “Jamming transition and inherent structures of hard spheres and disks,” *Physical review letters* **109**, 205701 (2012).
- [9] Misaki Ozawa, Ludovic Berthier, and Daniele Coslovich, “Exploring the jamming transition over a wide range of critical densities,” *SciPost Physics* **3**, 027 (2017).
- [10] O Reynolds, “Experiments showing dilatancy, a property of granular material, possibly connected with gravitation,” *Proc. R. Inst. GB* **11**, 12 (1886).
- [11] Varghese Babu, Deng Pan, Yuliang Jin, Bulbul Chakraborty, and Srikanth Sastry, “Is friction essential for dilatancy and shear jamming in granular matter?” (2020), [arXiv:2003.08815](https://arxiv.org/abs/2003.08815).
- [12] Dapeng Bi, Jie Zhang, Bulbul Chakraborty, and Robert P Behringer, “Jamming by shear,” *Nature* **480**, 355 (2011).
- [13] HA Vinutha and Srikanth Sastry, “Disentangling the role of structure and friction in shear jamming,” *Nature Physics* **12**, 578 (2016).
- [14] Ryohei Seto, Abhinendra Singh, Bulbul Chakraborty, Morton M Denn, and Jeffrey F Morris, “Shear jamming and fragility in dense suspensions,” *arXiv preprint arXiv:1902.04361* (2019).
- [15] Nishant Kumar and Stefan Luding, “Memory of jamming—multiscale models for soft and granular matter,” *Granular Matter* **18**, 58 (2016).
- [16] Pallabi Das, Srikanth Sastry, *et al.*, “Unified phase diagram of reversible-irreversible, jamming and yielding transitions in cyclically sheared soft sphere packings,” *arXiv preprint arXiv:1907.08503* (2019).
- [17] Yiqiu Zhao, Jonathan Barés, Hu Zheng, Joshua ES Socolar, Robert P Behringer, *et al.*, “Shear-jammed, fragile, and steady states in homogeneously strained granular materials,” *Physical review letters* **123**, 158001 (2019).
- [18] Thibault Bertrand, Robert P Behringer, Bulbul Chakraborty, Corey S O’Hern, and Mark D Shattuck, “Protocol dependence of the jamming transition,” *Physical Review E* **93**, 012901 (2016).
- [19] Marco Baity-Jesi, Carl P Goodrich, Andrea J Liu, Sidney R Nagel, and James P Sethna, “Emergent so(3) symmetry of the frictionless shear jamming transition,” *Journal of Statistical Physics* **167**, 735–748 (2017).
- [20] Ludovic Berthier, Daniele Coslovich, Andrea Ninarello, and Misaki Ozawa, “Equilibrium sampling of hard spheres up to the jamming density and beyond,” *Phys. Rev. Lett.* **116**, 238002 (2016).
- [21] Yuliang Jin, Pierfrancesco Urbani, Francesco Zamponi, and Hajime Yoshino, “A stability-reversibility map unifies elasticity, plasticity, yielding, and jamming in hard sphere glasses,” *Science advances* **4**, eaat6387 (2018).
- [22] Salvatore Torquato and Frank H Stillinger, “Jammed hard-particle packings: From kepler to bernal and beyond,” *Reviews of modern physics* **82**, 2633 (2010).
- [23] Patrick Charbonneau, Jorge Kurchan, Giorgio Parisi, Pierfrancesco Urbani, and Francesco Zamponi, “Fractal free energy landscapes in structural glasses,” *Nature communications* **5**, 3725 (2014).
- [24] Farhang Radjai, Dietrich E Wolf, Michel Jean, and Jean-

- Jacques Moreau, “Bimodal character of stress transmission in granular packings,” *Physical review letters* **80**, 61 (1998).
- [25] Paul J Steinhardt, David R Nelson, and Marco Ronchetti, “Bond-orientational order in liquids and glasses,” *Physical Review B* **28**, 784 (1983).
- [26] Francois Boyer, Elisabeth Guazzelli, and Olivier Pouliquen, “Unifying suspension and granular rheology,” *Physical Review Letters* **107**, 188301 (2011).
- [27] Ivo R Peters, Sayantan Majumdar, and Heinrich M Jaeger, “Direct observation of dynamic shear jamming in dense suspensions,” *Nature* **532**, 214 (2016).
- [28] Tomaso Aste, Mohammad Saadatfar, and TJ Senden, “Geometrical structure of disordered sphere packings,” *Physical Review E* **71**, 061302 (2005).
- [29] Corentin Coulaix, Antoine Seguin, and Olivier Dauchot, “Shear modulus and dilatancy softening in granular packings above jamming,” *Physical review letters* **113**, 198001 (2014).
- [30] Patrick Charbonneau, Atsushi Ikeda, Giorgio Parisi, and Francesco Zamponi, “Glass transition and random close packing above three dimensions,” *Physical review letters* **107**, 185702 (2011).
- [31] Wenwei Liu, Yuliang Jin, Sheng Chen, Hernán A Makse, and Shuiqing Li, “Equation of state for random sphere packings with arbitrary adhesion and friction,” *Soft matter* **13**, 421–427 (2017).
- [32] Ludovic Berthier, Patrick Charbonneau, Daniele Coslovich, Andrea Ninarello, Misaki Ozawa, and Sho Yaida, “Configurational entropy measurements in extremely supercooled liquids that break the glass ceiling,” *Proceedings of the National Academy of Sciences*, 201706860 (2017).
- [33] Yuliang Jin and Hernán A Makse, “A first-order phase transition defines the random close packing of hard spheres,” *Physica A: Statistical Mechanics and its Applications* **389**, 5362–5379 (2010).
- [34] Corrado Rainone, Pierfrancesco Urbani, Hajime Yoshino, and Francesco Zamponi, “Following the evolution of hard sphere glasses in infinite dimensions under external perturbations: Compression and shear strain,” *Physical review letters* **114**, 015701 (2015).
- [35] Corrado Rainone and Pierfrancesco Urbani, “Following the evolution of glassy states under external perturbations: the full replica symmetry breaking solution,” *Journal of Statistical Mechanics: Theory and Experiment* **2016**, 053302 (2016).
- [36] Silvio Franz and Giorgio Parisi, “Recipes for metastable states in spin glasses,” *Journal de Physique I* **5**, 1401–1415 (1995).
- [37] Alain Barrat, Silvio Franz, and Giorgio Parisi, “Temperature evolution and bifurcations of metastable states in mean-field spin glasses, with connections with structural glasses,” *Journal of Physics A: Mathematical and General* **30**, 5593 (1997).
- [38] Florent Krzakala and Lenka Zdeborová, “Following gibbs states adiabatically the energy landscape of mean-field glassy systems,” *EPL (Europhysics Letters)* **90**, 66002 (2010).
- [39] Florent Krzakala and Lenka Zdeborová, “Performance of simulated annealing in p-spin glasses,” in *Journal of Physics: Conference Series*, Vol. 473 (IOP Publishing, 2013) p. 012022.
- [40] Giampaolo Folena, Silvio Franz, and Federico Ricci-Tersenghi, “Memories from the ergodic phase: the awkward dynamics of spherical mixed p-spin models,” *arXiv preprint arXiv:1903.01421* (2019).
- [41] Yuliang Jin and Hajime Yoshino, “Exploring the complex free-energy landscape of the simplest glass by rheology,” *Nature Communications* **8** (2017).
- [42] Andrea Ninarello, Ludovic Berthier, and Daniele Coslovich, “Models and algorithms for the next generation of glass transition studies,” *Physical Review X* **7**, 021039 (2017).
- [43] Daniele Coslovich, Ludovic Berthier, and Misaki Ozawa, “Exploring the jamming transition over a wide range of critical densities,” *SciPost Physics* **3**, 027 (2017).
- [44] Ludovic Berthier, Patrick Charbonneau, Yuliang Jin, Giorgio Parisi, Beatriz Seoane, and Francesco Zamponi, “Growing timescales and lengthscales characterizing vibrations of amorphous solids,” *Proceedings of the National Academy of Sciences* **113**, 8397–8401 (2016).
- [45] Erik Bitzek, Pekka Koskinen, Franz Gähler, Michael Moseler, and Peter Gumbsch, “Structural relaxation made simple,” *Physical review letters* **97**, 170201 (2006).
- [46] AW Lees and SF Edwards, “The computer study of transport processes under extreme conditions,” *Journal of Physics C: Solid State Physics* **5**, 1921 (1972).
- [47] Monica Skoge, Aleksandar Donev, Frank H Stillinger, and Salvatore Torquato, “Packing hyperspheres in high-dimensional euclidean spaces,” *Physical Review E* **74**, 041127 (2006).
- [48] Pierfrancesco Urbani and Francesco Zamponi, “Shear yielding and shear jamming of dense hard sphere glasses,” *Physical review letters* **118**, 038001 (2017).
- [49] Ada Altieri and Francesco Zamponi, “Mean-field stability map of hard-sphere glasses,” *Physical Review E* **100**, 032140 (2019).
- [50] Carl F Schreck, Robert S Hoy, Mark D Shattuck, and Corey S O’Hern, “Particle-scale reversibility in athermal particulate media below jamming,” *Physical Review E* **88**, 052205 (2013).
- [51] Takeshi Kawasaki and Ludovic Berthier, “Macroscopic yielding in jammed solids is accompanied by a nonequilibrium first-order transition in particle trajectories,” *Physical Review E* **94**, 022615 (2016).
- [52] Francesco Zamponi, “Surfing on (or drowning under?) the threshold,” *arXiv preprint arXiv:1903.01421* (2019).
- [53] Sheng Chen, Thibault Bertrand, Weiwei Jin, Mark D Shattuck, and Corey S O’Hern, “Stress anisotropy in shear-jammed packings of frictionless disks,” *Physical Review E* **98**, 042906 (2018).
- [54] Walter Mickel, Sebastian C Kapfer, Gerd E Schröder-Turk, and Klaus Mecke, “Shortcomings of the bond orientational order parameters for the analysis of disordered particulate matter,” *The Journal of chemical physics* **138**, 044501 (2013).
- [55] Tommaso Castellani and Andrea Cavagna, “Spin-glass theory for pedestrians,” *Journal of Statistical Mechanics: Theory and Experiment* **2005**, P05012 (2005).
- [56] Michio Otsuki and Hisao Hayakawa, “Critical scaling near jamming transition for frictional granular particles,” *Physical Review E* **83**, 051301 (2011).
- [57] Sebastian C Kapfer, Walter Mickel, Klaus Mecke, and Gerd E Schröder-Turk, “Jammed spheres: Minkowski tensors reveal onset of local crystallinity,” *Physical Review E* **85**, 030301(R) (2012).
- [58] Laurent Corte, Paul M Chaikin, Jerry P Gollub, and

- David J Pine, “Random organization in periodically driven systems,” *Nature Physics* **4**, 420–424 (2008).
- [59] Kentaro Nagasawa, Kunimasa Miyazaki, and Takeshi Kawasaki, “Classification of the reversible–irreversible transitions in particle trajectories across the jamming transition point,” *Soft matter* **15**, 7557–7566 (2019).